ACS Catalysis

pubs.acs.org/acscatalysis
Research Article

Theoretical Study of the Arachidonic Acid Conversion into Leukotriene A_4 Catalyzed by Human 5-Lipoxygenase: Hydroperoxidation and Epoxidation Mechanisms and Arachidonic Acid Active Site Access

Alejandro Cruz, Àngels González-Lafont, and José M. Lluch*

Cite This: ACS Catal. 2024, 14, 637−656
Read Online

ACCESS | Metrics & More | Article Recommendations | Supporting Information

ABSTRACT: Inflammation is at the base of many different diseases. Leukotrienes (LTs) are pro-inflammatory mediators derived from arachidonic acid (AA), which play significant roles in acute inflammation. Lipoxins are specialized pro-resolving mediators (SPMs), also formed from AA, that promote the resolution of acute inflammation. However, if resolution fails, chronic inflammatory processes might develop. The enzyme human-5-lipoxygenase (5-LOX) catalyzes the biosynthesis of leukotriene named LTA_4 but also intervenes in the formation of the lipoxin LXA_4. These two biological functions have made the 5-LOX isoform a current target for pharmaceutical investigations in several inflammatory-based diseases searching for inhibitors that block the leukotriene reaction pathway but not lipoxin's formation. However, the development of those selective inhibitors has been hampered by the lack of a crystal structure of human 5-LOX. In this work, we have built a complete solvated model of the human-5-LOX: AA Michaelis complex using, as initial coordinates, the human 5-LOX structure from the AlphaFold protein structure database. We aim to analyze at the molecular level the overall catalytic mechanism of 5-LOX that first converts AA into 5(*S*)-HpETE through a hydroperoxidation reaction and, second, transforms this hydroperoxide into LTA_4 following an epoxidation process. Methodologically, we have performed molecular dynamics simulations and quantum mechanics/molecular mechanics calculations. The free energy profiles for AA entrance into the 5-LOX's binding cavity have been calculated by steered molecular dynamics. This detailed molecular information can explain human-5-LOX's in vitro activity (without the presence of the membrane-embedded 5-lipoxygenase-activating protein) and help to design selective inhibitors favoring inflammation resolution.

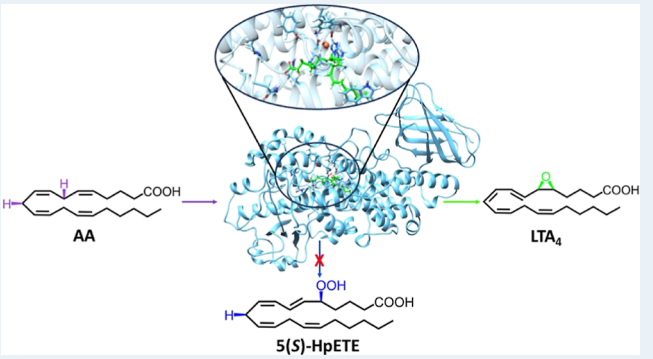

KEYWORDS: *leukotriene A_4, human 5-lipoxygenase, arachidonic acid active site access, epoxidation mechanism, quantum mechanics/molecular mechanics calculations, steered molecular dynamics simulations*

1. INTRODUCTION

Chronic inflammatory diseases have been recognized as the leading cause of death in the world today, with more than 50% of all deaths resulting from inflammation-related diseases.[1] Physical injuries or microbial infections trigger a physiological innate response that occurs in vascularized tissues to protect the host, which is needed for maintaining health, thus starting acute inflammation, whose cardinal signs are heat, pain, tissue swelling, redness, and impaired function.[2] It is initiated by neutrophils, eosinophils, and M1-polarized macrophages, releasing prostaglandins and leukotrienes (LTs).[3] These pro-inflammatory lipid mediators derive from the arachidonic acid (AA, 5*Z*,8*Z*,11*Z*,14*Z*-eicosatetraenoic acid) by the action of the key pro-inflammatory enzymes, cyclooxygenase-2 and 5-lipoxygenase (5-LOX), respectively.[4]

Acute inflammation, as a response of the immune system to a damaging attack, should be localized and self-limited, and return to homeostasis. If not resolved, organ pathologies leading to chronic inflammatory phenotypes can result. It is nowadays recognized that the resolution of inflammation is an active mechanism with a biosynthetic shift from pro-inflammatory to pro-resolution lipid mediators, the specialized pro-resolving mediators (SPMs), enzymatically derived from

Received: October 16, 2023
Revised: December 13, 2023
Accepted: December 14, 2023
Published: December 29, 2023

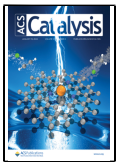

https://doi.org/10.1021/acscatal.3c04954
ACS Catal. 2024, 14, 637−656

poly unsaturated fatty acids.[4−9] Lipoxins (from lipoxygenase interaction products) were the first class of SPMs discovered.[10]

Lipoxygenases are a family of nonheme iron-containing dioxygenases that catalyze highly regio- and stereospecific hydroperoxidation of polyunsaturated fatty acids holding 1,4-*Z*,*Z*-pentadiene units.[11−14] 5-lipoxygenases are the most interesting but also the most elusive of human lipoxygenases. First, they are bifunctional catalysts. 5-LOX catalyzes the hydroperoxidation of carbon C_5 of AA, producing 5*S*-hydroperoxy-6*E*,8*Z*,11*Z*,14*Z*-eicosatetraenoic acid (5-HpETE). Then, 5-LOX catalyzes the formation of the unstable epoxide intermediate Leukotriene A_4 (LTA_4, 5*S*,6*S*-epoxy-7*E*,9*E*,11*Z*,14*Z*-eicosatetraenoic acid) by dehydration of 5-HpETE, involving an initial abstraction of its pro-*R* hydrogen at C_{10}.[13] Other enzymes transform LTA_4 into several pro-inflammatory LTs that act as potent chemotactic mediators that promote the recruitment of polymorphonuclear leukocytes to the inflamed region in the acute inflammation.[15−18] Second, in the opposite direction, 5-LOX is also involved in the biosynthesis of anti-inflammatory SPMs, like lipoxins. In effect, lipoxins can be formed from AA via transcellular biosynthesis through the sequential actions of 5-LOX and 12-LOX (or 15-LOX-1), using LTA_4 as an intermediate, or by the action of 15-LOX-1 in 5-LOX-bearing cells.[4]

The 5-LOX protein has not been crystallized so far. Newcomer and co-workers[19] identified a destabilizing Lys-rich sequence close to the C-terminus that prevents crystallization. Mutation of that Lys653−Lys654−Lys655 sequence to a Glu−Gln−Leu sequence, along with the removal of Ca^{2+} binding and putative membrane-insertion amino acids (Δ40 to 44GlySer, Trp13Glu, Phe14His, Trp75Gly, and Leu76Ser), and two Cys mutations (Cys240Ala and Cys561Ala) increased the stability of the protein and made it possible the first crystal structure of an engineered human-5-LOX at 2.4 Å resolution, the so-called Stable-5-LOX. Stable-5-LOX also catalyzes the formation of 5-HpETE and LTA_4.

An elongated helix α2 with at least six turns appears in the LOX isoforms in animals, but in Stable 5-LOX, it is a broken helix with segments of at most three-helical turns that form a v-like structure. With this position of the helix α2 the aromatic side chains of the residues Tyr181 and Phe177 cork the cavity at one end of the elongated cavity,[19,20] thus obstructing the way of AA into the active site. It is called a closed conformation, in contrast to the elongated, open conformation of the helix α2 in other animal LOXs. Thus, a very intriguing point is how AA gains access to the active site. Two alternatives have been experimentally proposed.[19] The first one involves removal of the FY cork, so AA could enter the cavity with its carboxylate end first, leading to an inverse alignment (head-first) of the substrate relative to that for the 15*S*-LOX and 8*R*-LOX but being consistent with the *S*-stereochemistry of the human-5-LOX products. The second possibility would require a rotamer shift of Trp147 at the opposite end of the cavity. In this case, the AA enters the methyl end first but also leads to the same head-first alignment. However, the mutation to a smaller residue (Trp147Leu) led to a significant reduction of the enzyme's activity, stability, and product specificity, which seemed to be inconsistent with the role of Trp147 as an access portal.[21]

When cells are stimulated to release intracellular Ca^{2+}, the translocation of cytosolic phospholipase A_2 and 5-LOX to the nuclear membrane is triggered. Phospholipase A_2 mediates the release of AA from membrane phospholipids, and a small membrane protein, 5-lipoxygenase-activating protein (FLAP) transfers AA to 5-LOX.[13,20,22] It has been proposed[20,23] that the open conformation would increase the ability of 5-LOX to convert 5-HpETE into LTA_4 and that this conformation is likely the one presented by 5-LOX when interacting with membrane-embedded FLAP. On the other hand, human-5-LOX can also produce LTA_4 in vitro (in the absence of the membrane-embedded FLAP) from AA sequentially (hydroperoxidation + epoxidation).[16]

As explained above, LTs are lipid mediators with a very important pathogenic role in inflammatory-based diseases. Massive efforts have been dedicated for many years to develop new therapeutics based on efficient 5-LOX inhibitors, specially facing the challenge of designing inhibitors that suppress the formation of LTs without lowering the production of lipoxins.[22] To this aim, the lack of a crystal structure of 5-LOX has been a big obstacle, thus preventing a complete understanding at the molecular level of the mechanism of the reactions catalyzed by 5-LOX. Several years ago, some of us used Stable-5-LOX to find the binding modes for AA inside the cavity of the enzyme. However, we were unable to discover any stable binding mode that could clearly exhibit the predominant 5-lipoxygenating reactivity.[24] In this work, the AlphaFold protein structure database for human-5-LOX has been used, thus presenting the first available model of the human-5-LOX: AA Michaelis complex that leads to rationalize the reaction mechanism of the enzyme. In addition, molecular dynamics (MD) simulations plus quantum mechanics/molecular mechanics calculations have been carried out to get a complete, detailed mechanism at the molecular level of the conversion of AA into LTA_4 catalyzed by human-5-LOX in the absence of the membrane-embedded FLAP (thus mimicking the in vitro behavior). Special attention has been paid to discussing the AA active site access using steered MD (SMD) simulations.

In the next step, still beyond the scope of the present work, we plan to extend this study to the complete system including the membrane-embedded FLAP. Anyway, we hope the results already obtained here can stimulate the progress of new experimental work.

2. COMPUTATIONAL METHODS

2.1. System Setup. Due to the nonavailability of an experimental structure for the wild-type human 5-LOX, the structure provided by the AlphaFold protein structure database (UniProt P09917)[25,26] has been used. Thus, the AlphaFold numbering has been employed for protein residues.

The Fe(III)−OH^- cofactor of the catalytic center has been added because it is not contained in the monomeric structure taken from AlphaFold. On the other hand, the spatial arrangement and conformation of the residues Val672, Ala673, and Ile674 (terminal residue) have been modified to allow the terminal carboxyl group of the latter residue to coordinate to the iron atom of the Fe(III)−OH^- cofactor. Cartesian coordinates for the iron atom and the heavy atoms of Val672, Ala673, and Ile674 have been obtained by means of an overlap of the structure provided by AlphaFold for the wild-type human 5-LOX with one of the available crystallographic structures for the human Stable-5-LOX (PDB code 3O8Y).[19] However, the OH^- group of the Fe(III)−OH^- cofactor has been placed manually taking into account the position of the rest of the members of the coordination sphere of the iron atom. The resulting structure from the aforementioned procedure has been protonated with the H++ web server,[27,28]

https://doi.org/10.1021/acscatal.3c04954
ACS Catal. 2024, 14, 637−656

using a pH = 7.5 for titratable residues. The protonation state for the coordination sphere of the iron atom was corrected by hand to ensure a correct description of it. That pH value has been used according to available experimental data of the catalytic activity of the wild-type human 5-LOX with AA as a substrate.[16] The pK_a values of the NH_3^+ group of Lys654, Lys655, and Lys656 turn out to be 10.4, 10.6, and 9.9, respectively, that is, more than two points above the desired pH (7.5). This initial structure of human-5-LOX model corresponds to the situation in which Lys655 is hydrogen bonded to Glu651, while Lys654 is pointing to the solvent. Although the calculated pK_a values depend on each particular structure, taking into account the considerable difference between the pK_a values of Lys654, Lys655, and Lys656 and the desired pH, it can be concluded that these three lysines are mainly protonated.

2.2. Docking Calculations. The GOLD5.8.0[29] program was used to perform the AA docking calculations within the cavity of the human-5-LOX, where the MD relaxed structure resulting from the aforementioned procedure was used as a receptor. The binding site was defined as a 20 Å radius sphere centered on the iron atom. The receptor remained rigid, but total flexibility was given to the ligand during the conformational exploration. The GOLD's option to take into account the interactions of organic ligands with metal ions in metalloenzymes was activated, but the docking exploration was restricted to hexacoordinated geometries of iron. In order to ensure an extensive conformational exploration of AA the most efficient genetic algorithm was employed. The ChemScore fitness function was used to estimate the Gibbs binding energies of this substrate.

2.3. MD Simulations. The different systems were assembled using the procedure recommended by the AMBER software package.[30] The force field ff14SB[31] was used for the protein atoms. Instead, the force field parameters for AA[32] and the iron atom with its first coordination sphere (His368, His373, His551, Asn555, Ile674, and the OH^- group) were recovered from a previous work,[33] while the specific parameters of 5(*S*)-HpETE were developed here (see the Supporting Information). The calculations to generate those specific parameters were carried out following the standard protocol in AMBER with antechamber and parmchk2 modules. The GAFF2[30,34] library was used as the source for all these parameters. The B3LYP/6-31G(d) level of theory was employed to optimize the 5(*S*)-HpETE structure and its atomic charges were assigned using the Merz−Kollman RESP procedure.[35] Finally, the protonation states of AA and 5(*S*)-HpETE were also established by hand to ensure that they matched the protonation states under physiological conditions.

All performed MD simulations followed the same protocol, the only difference between them was the starting structure and the length of the production period. After combining the corresponding files, the different systems were solvated with an orthorhombic box of pre-equilibrated TIP3P waters[36] and their total charge was neutralized by adding sodium cations using the tLeap program. The resulting systems contained about 107,500 atoms, of which about 10,900 belonged to the enzyme. The remaining atoms represent water molecules and sodium cations. All the MD simulations were calculated with the AMBER 20 GPU (CUDA) version of the PMEMD software package.[37,38] Initially, the system was submitted to 22,000 energy minimization steps using the steepest-descent method to avoid close contacts. In the first 6000 steps, harmonic restraints were applied to the protein and substrate atoms (when the substrate is included in the system) with a force constant of 5.0 kcal mol^{-1} $Å^{-2}$, so that only the solvent and ions were relaxed. In the next 6000 steps, harmonic restraints were applied to the protein backbone and the substrate heavy atoms (when the substrate is included in the system) with a force constant of 5.0 kcal mol^{-1} $Å^{-2}$. In the last 10,000 steps, the entire system was kept free of restraints. After this, MD simulations were carried out using periodic boundary conditions. The system was gradually heated from 0 to 300 K for a period of 200 ps. Next, an MD run of 1 ns, at constant temperature and pressure (300 *K*, 1 bar), has been calculated to adjust the volume of the orthorhombic box so that a density of around 1 g cm^{-3} is reached. Throughout the heating and compressing, harmonic restraints were applied to the protein backbone and substrate heavy atoms (if present) with a force constant of 5.0 kcal mol^{-1} $Å^{-2}$, whereas no restraints were applied to the rest of the system. The temperature was controlled by Langevin dynamics (with a collision frequency of 3.0 ps^{-1}),[39] while the pressure was adjusted by the Berendsen barostat.[40] Then, an equilibration stage of 10 ns was performed at constant temperature (300 *K*) and volume. Finally, a production period was calculated within the same isothermal-isochoric ensemble. Throughout the MD trajectory a time step of 2 fs was used and all bonds and angles containing hydrogen atoms were restricted using the SHAKE[41] algorithm. The particle-mesh Ewald (PME)[42,43] procedure is used to handle long-range electrostatic interactions. The nonbonding interactions have been calculated with a cutoff of 9 Å. For PME, the cutoff is used to limit direct space sum. For Lennard-Jones interactions, a long-range dispersion correction based on an analytical integral assuming an isotropic, uniform bulk particle distribution beyond the cutoff is added to the van der Waals energy. The analysis of the MD simulations has been carried out with AmberTools20.[30] As a starting structure for the MD simulation of the human-5-LOX-empty system, the structure of human 5-LOX provided by AlphaFold after having applied the aforementioned procedure was used. A production period of 500 ns was carried out. This MD simulation had the aim of relaxing the human-5-LOX-empty system. A typical structure of that MD simulation was employed as a receptor for the AA docking calculations in the cavity of the human-5-LOX-empty system. Next, the best docking solution of the AA inside this cavity compatible with its subsequent reactivity was selected as the starting structure for the 200 ns MD simulation of the human-5-LOX:AA Michaelis complex. Finally, the QM/MM optimized structure of 5(*S*)-HpETE inside the 5-LOX cavity coming from the initial hydroperoxydation mechanism (see next section) was used as the starting structure for the 200 ns MD simulation of the human-5-LOX:5(*S*)-HpETE complex.

2.4. QM/MM Calculations. The modular program package ChemShell[44,45] was used to perform the QM/MM calculations. TURBOMOLE[46] was employed for DFT calculations, whereas AMBER force fields were employed for the MM calculations using the DL_POLY[47] module in ChemShell. An electrostatic embedding scheme[48] was employed to treat the interaction between the QM and MM subsystems. Moreover, a link atom scheme was adopted to describe the QM/MM boundary by using the charge shift model[49] and cutoffs were not introduced to treat the nonbonding MM and QM/MM interactions.[50] The QM/MM optimizations have been carried out by employing the limited-memory Broyden−Fletcher−Goldfard−Shanno[51,52] algorithm for energy minimizations.

https://doi.org/10.1021/acscatal.3c04954
ACS Catal. 2024, 14, 637−656

This algorithm is implemented in the DL_FIND library of ChemShell[53] geometry optimizations. In order to carry out the QM/MM calculations, some structures that seemed suitable to undergo the 5-LOX enzymatic process were selected from the MD simulation of the human-5-LOX:AA Michaelis complex. For each selected structure, all water molecules outside a volume of 17 Å radius centered on the substrate molecule were removed. The active region was defined by all residues and water molecules inside a 15 Å radius sphere centered on C_5 of the ligand molecule. This region, which contains around 2100 atoms, was kept free, whereas the remaining atoms were kept frozen. Roughly 12,600 atoms were taken into account in each QM/MM calculation.

The QM region was described by the B3LYP hybrid functional.[54] The 6-31G(d) People basis set[55] was employed for the C, H, O, and N atoms, while the LANL2DZ basis set[56] was used for the Fe atom. The LANL2DZ basis set is a relatively reduced basis set that combines an effective core potential and a valence basis set of double-ζ quality. In general, this basis set must be used with caution, but it has been shown that can be employed to describe the Fe atom in many lipoxygenase reactions with acceptable results.[57−60] In the Supporting Information (see Table S1), we have shown that the relative energies presented in this paper does not significantly change if a single-point Grimme D3(BJ)-dispersion correction is calculated.[61] As for the pro-*S* hydrogen abstraction from C_7, the QM region (see Figure 1) was defined

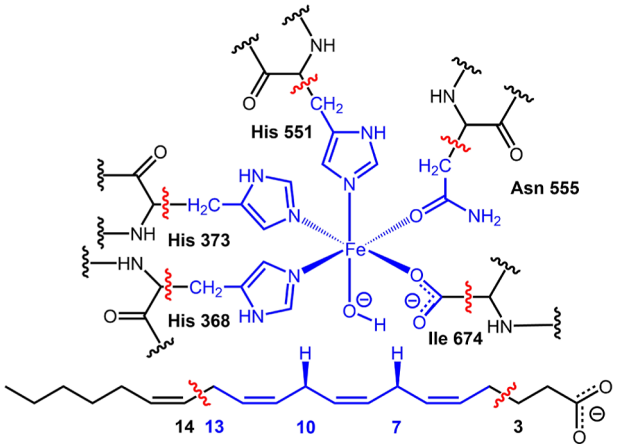

Figure 1. QM/MM partition for hydrogen abstraction of C_7. QM atoms are depicted in blue. The boundary between the QM and MM regions is indicated by red wavy lines. An oxygen molecule must be added to the QM region for the rest of the stages of the enzymatic process that human-5-LOX catalyzes with AA as a substrate.

by all atoms of the lipid substrate which are found between C_3 and C_{14}, 11 atoms for each His residue in the iron coordination sphere (His368, His373, and His551), 8 atoms of the Asn residue (Asn555) in the iron coordination sphere, 3 atoms of the Ile terminal residue (Ile 674) in the iron coordination sphere, and the Fe(III)−OH^- cofactor. For the rest of the human-5-LOX enzymatic process steps, this region was enlarged by an oxygen molecule. In all cases, a multiplicity corresponding to a sextet was used.[62] The net charge of the QM region is 1 au. Seven link atoms were employed, five between the bonds Cα-QM atoms of the five residues in the iron coordination sphere and two bonded to the aliphatic carbon atoms of the lipid substrate (placed between C_3−C_4 and C_{13}−C_{14}).

The potential energy profiles have been calculated by performing several energy optimizations imposing harmonic restraints on the reaction coordinate, with an increment of 0.1 Å or smaller at each step. The reactant and product structures for each reaction step have been located by minimizing the potential energy of the corresponding geometries in each potential energy profile. The maximum energy point for each potential energy profile has been directly taken as the corresponding transition state structure.

2.5. Oxygen Access Channels. Concerning the oxygenation step, the channels through which oxygen can access inside the enzyme human 5-LOX have been searched using the plugin Caver3.0.3[63] of PyMol.[64] We have only analyzed the structure that presented a lower potential energy barrier for the abstraction of pro-*S* hydrogen of C_7 among the structures that were considered suitable to undergo the 5-LOX enzymatic process. For the calculation of these channels, C_5 of AA, which is the carbon atom where the oxygenation occurs, was chosen as the starting point, and the default value was selected for the rest of the channel's parameters, except for the minimum test radius and the desired radius, which have been set to a value of 0.6 and 2 Å, respectively. The aim of modifying these two parameters is to locate all channels through which the oxygen molecule can approach to C_5 in whichever orientation, in other words, to allow the oxygen molecule to rotate along its approach to C_5. All visualizations and representations have been made with the VMD[65] and UCSF Chimera[66] programs.

2.6. SMD Simulations. The Caver 3.0 program[63] was employed to study possible channels through which AA can leave the enzyme cavity. 40 structures uniformly distributed of the MD simulation of the human-5-LOX:AA Michaelis complex were selected to this purpose. In this case, the whole AA was chosen as a starting point to ensure that all channels arise from the substrate. The default value was selected for the rest of the channel's parameters, except for shell depth and number of approximating balls which were set to 3 Å and 12, respectively. These two values were modified to take into account the substrate depth inside the human-5-LOX pocket and to prevent channels from being too short, respectively. According to Caver results, three possible outgoing channels for AA were identified. For each channel, a representative ensemble of structures was selected where the considered channel was open, and for each one of these structures, a SMD[38] simulation was performed in which the AA departure to solution is achieved using a proper stretching coordinate. All the SMD simulations were carried out employing the AMBER 20 software package[30] in the *NVT* ensemble. Again, the temperature was kept constant at 300 *K*, the time step was set to 2 fs, all bonds and angles containing hydrogen atoms were restricted using the SHAKE algorithm, and nonbonding interactions were calculated using a cutoff of 9 Å. The pulling velocity was fixed to 10 Å ns^{-1} and the force constant was fixed to 50 kcal mol^{-1} $Å^{-2}$. With the aim of reducing statistical mistakes related to a poor sampling, the second-order cumulant expansion[67−70] was employed to calculate the potential of mean force (PMF) for each possible outgoing channel for AA from the corresponding SMD simulations which do not exhibit an excessive cumulated work to achieve the AA departure to solution.

https://doi.org/10.1021/acscatal.3c04954
ACS Catal. 2024, 14, 637−656

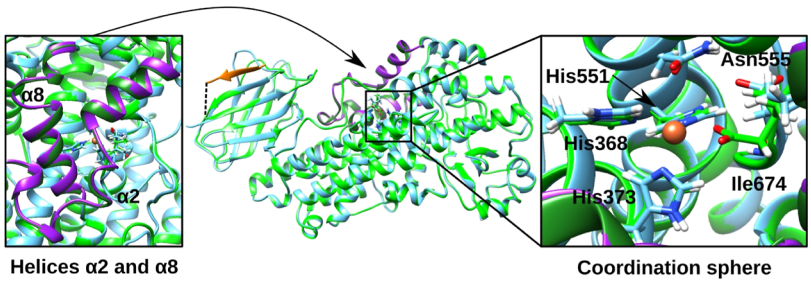

Figure 2. Overlap between human-5-LOX provided by AlphaFold (in blue) and human Stable-5-LOX (PDB code 3O8Y) (in green). The additional β-strand of human Stable-5-LOX is represented in orange (this structure lacks the loop that joins this β-strand with the rest of the *N*-terminal domain and the union of these two regions has been indicated with a dashed black line). For greater visibility, in the left panel the helices α2 and α8 have been represented from another perspective, in violet for human-5-LOX and in dark green for human Stable-5-LOX. The panel on the right contains an enlarged image of the coordination sphere of Fe for both structures where it can be seen that the terminal Ile674 of human-5-LOX cannot coordinate to Fe, while the same residue of human Stable-5-LOX can.

3. RESULTS AND DISCUSSION

3.1. Comparison between Human-5-LOX (AlphaFold) and Human Stable-5-LOX. First, we have compared the structure provided by AlphaFold for the human-5-LOX (UniProt P09917)[25,26] with the monomer A of the human Stable 5-LOX (PDB code 3O8Y).[19] The superposition of both structures (Figure 2) shows that they are very similar to each other. The most notable difference is found in the *N*-terminal domain, where human Stable-5-LOX contains an additional β-strand, which would help the crystallization of this mutant, with respect to the same domain of the structure of human-5-LOX. The C-terminal domain is practically identical for both structures, including the helices α2 and α8 that exhibit a particular secondary structure that is characteristic only of the 5-LOX isoform. An interesting difference between the two structures is the spatial and conformational arrangement of the residues Val672, Ala673, and Ile674: in the case of human-5-LOX, the terminal Ile674 cannot coordinate to the iron atom that is responsible for enzymatic catalysis, which justifies the procedure we have used to build our structure for human-5-LOX (see above). That great similarity between both C-terminal domains causes that the shape of the cavity of both structures is also much alike.

Throughout the MD simulation, our built human-5-LOX model breathes and adapts to be solvated. In the region containing the three consecutive lysines (residues 654−656), which are in the last turn of the helix α that precedes the carboxylate group of the terminal Ile674, Lys654, and Lys655 compete to form hydrogen bonds with the carboxylate group of the side chain of Glu651 (see Figure 3). Most of the time, the NH_3^+ group of the Lys654 side chain forms a hydrogen bond with Glu651 (panel A of Figure 3), whereas the NH_3^+ group of the Lys655 side chain points to the solvent, in such a way that the last turn of that terminal helix α is slightly deformed. Conversely, that helix α has a well-defined shape when Lys655 is hydrogen bonded to Glu651 (panel B of Figure 3). The transition between these two conformations of Lys654 and Lys655 generates a vibration that propagates through both ends of that terminal helix α. Lys656 remains forming hydrogen bonds with the oxygen atom of the Arg652 backbone. These three lysines are precisely those that are mutated in human Stable-5-LOX with the aim of providing stability to the enzyme and making its crystallization possible. Our MD simulation results suggest the reason why the mutation of these three consecutive lysines gives stability to the enzyme.

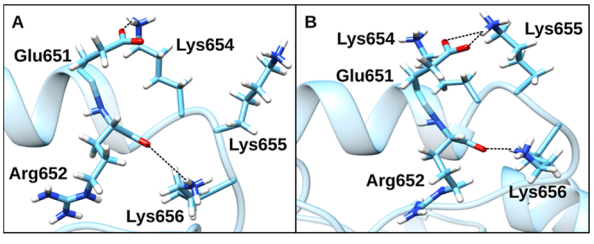

Figure 3. Representation of the two conformations of Lys654 and Lys655 of the terminal helix α. Lys654 (panel A) or Lys655 (panel B) connect with the carboxylate group of the side chain of Glu651. Hydrogen bonds are indicated by dashed black lines.

3.2. Molecular Docking Simulations of AA. Docking calculations of AA within the human-5-LOX cavity after a first MD relaxation have produced six AA structural clusters, the best of which is the most populated. In the first, second, third, fourth, and sixth clusters, the AA carboxylate group is on the same side of Trp148 (see Figure S1). However, all these five clusters have two important drawbacks: (1) the carboxylate group of AA is not held by any strong hydrogen bond, which suggests that the AA pose is not very stable and will present great flexibility; (2) their distances from C_7, C_{10}, and C_{13} to the oxygen atom of the Fe(III)−OH^- cofactor are not compatible with the reactivity exhibited by human-5-LOX for AA (see Table 1). Conversely, in the fifth best cluster, the AA carboxylate group is on the opposite side (see Figures S1 and S2), and the distances C_7−OH, C_{10}−OH, and C_{13}−OH (see Table 1) are now compatible with the known reactivity. In addition, the carboxylate group for this fifth cluster presents a head-first orientation (in agreement with the available

Table 1. Distances from C_7, C_{10}, and C_{13} of AA to the Oxygen Atom of the OH^- Group of the Fe(III)−OH^- Cofactor for the Best Solution of Each One of the Six Clusters Obtained from the AA Docking Calculations Inside the Human-5-LOX Enzyme

cluster	d(C_7−OH^-) (Å)	d(C_{10}−OH^-) (Å)	d(C_{13}−OH^-) (Å)
1	10.17	7.21	4.21
2	7.66	4.64	3.10
3	5.85	3.12	3.17
4	7.77	4.58	3.34
5	4.23	3.30	5.54
6	6.47	3.29	4.37

https://doi.org/10.1021/acscatal.3c04954
ACS Catal. 2024, 14, 637−656

experimental information[19]) and is well anchored, since one of its oxygen atoms forms a hydrogen bond with the NH_2 group of the side chain of Asn426, and the other forms a hydrogen bond, somewhat less strong than the previous one, with the NH group of the skeleton of Val605, and interacts electrostatically in a favorable way with His601. Here, head/tail-first orientation will refer to the relative position of the carboxylate group of AA with respect to Lys410, which is assumed to have a similar role to Arg403 and Arg599 in rabbit 15-LOX-1 concerning substrate fixation. Thus, the tail-first orientation means that the carboxylate group of AA is directed toward the protein surface of the cavity where Lys410 is located, while head-first means the opposite orientation (the carboxylate pointing to the bottom of the cavity). The best solution of that fifth cluster will be used to start the MD simulation of the human-5-LOX:AA Michaelis complex.

3.3. MD Simulation of the Human-5-LOX:AA Michaelis Complex. In the equilibration stage of the MD simulation of the human-5-LOX:AA Michaelis complex AA reorganizes by placing the C_7 atom pointing to the OH^- group of the Fe(III)−OH^- cofactor with one of its hydrogen atoms well oriented to be abstracted, while C_{10} and C_{13} move away from that cofactor, which hinders the abstraction of hydrogens from these carbon atoms. Along the 200 ns of the production stage two periods can be distinguished, one of stabilization and the other of consolidation. During the stabilization period, the carboxylate group and the first carbon atoms of AA show great mobility, although the region of AA where C_7, C_{10}, and C_{13} are remains much more rigid. This period extends during the first 49 ns of the production stage and the carboxylate group interacts with many residues, especially Tyr182, Gln364, Thr365, His368, Asn426, Thr428, and Gln558, either forming hydrogen bonds or establishing electrostatic interactions. These interactions are generally quite weak and short-lived, although they can sometimes become very intense. In contrast, during the consolidation period (see Figure S3), the conformation of AA is relatively rigid and does not undergo sudden fluctuations. This is because the carboxylate group is quite fixed by the formation of hydrogen bonds with the triad Tyr182 (with the OH group of its side chain), Gln364 (with the NH_2 group of its side chain) and Asn426 (with the NH_2 group of its side chain), being the strongest interaction with the second residue.

As explained above,[13] conversion of AA to LTA_4 requires first the abstraction of H_{7proS} (for the hydroperoxidation process) and the subsequent abstraction of H_{10proR} (for the epoxidation process). Therefore, it is worth analyzing the evolution of the distances from C_7, C_{10}, C_{13} and the hydrogen atoms attached to the first two carbon atoms to the oxygen atom of the Fe(III)−OH^- cofactor throughout the MD simulation. Figure S4 shows that C_7 is almost always closer to the hydrogen acceptor oxygen atom than C_{10}, while C_{13} is always clearly farther away. The corresponding average distances C_7−OH^-, C_{10}−OH^-, and C_{13}−OH^- (Table 2) also reflect this trend. Based on a criterion of distances, it can be concluded that both the hydrogen abstraction from C_7 and C_{10} are viable, the first one being much easier. Conversely, hydrogen abstraction from C_{13} would not be possible. That is in accordance with the experimental reactivity.[71]

Regarding the hydrogen atoms, Table 2 and Figure S5 show that the H_{7proS} is much closer to the acceptor oxygen atom than H_{7proR}. On the other hand, the distances from H_{10proS} or H_{10proR} to that oxygen atom are similar. Thus, both the abstractions of H_{7proS} and H_{10proR} that take place experimentally seem to be feasible according to our MD calculations. To identify a precatalytic structure that can undergo both the abstraction of H_{7proS} and H_{10proR}, we have used a filter based on these two simultaneous conditions: (1) $d(H_{7proS}–OH) \leq 3.0$ Å and $d(H_{7proS}–OH) < d(C_7–OH)$; (2) $d(H_{10proR}–OH) \leq 5.0$ Å and $d(H_{10proR}–OH) < d(C_{10}–OH)$. It should be noted that for the hydrogen abstraction from C_{10} a less severe condition is imposed than for C_7 because, as mentioned above, C_7 is closer to the acceptor oxygen atom than C_{10}, and during the hydroperoxidation, the first process of the enzymatic mechanism of human-5-LOX, small motions of AA can occur that bring C_{10} closer to the hydrogen acceptor oxygen atom. Applying this filter, a total of 61 precatalytic structures have been obtained (3 of which have been randomly selected to try to carry out the initial abstraction of H_{7proS}), which represents a 0.31% of all structures of the MD simulation. This small generation of precatalytic structures is consistent with the fact that human-5-LOX is one of the slowest isoforms of the LOX family.[72]

Table 2. Average Distances of Interest from a Reactivity Point of View Corresponding to the 200 ns MD Simulation of the Human-5-LOX:AA Michaelis Complex along with Their Standard Deviations[a]

distance	average distances and standard deviations (in Å)
$d(C_7–OH^-)$	3.92 ± 0.48
$d(H_{7proS}–OH^-)$	3.58 ± 0.78
$d(H_{7proR}–OH^-)$	4.82 ± 0.62
$d(C_{10}–OH^-)$	5.76 ± 0.37
$d(H_{10proS}–OH^-)$	5.49 ± 0.45
$d(H_{10proR}–OH^-)$	5.94 ± 0.45
$d(C_{13}–OH^-)$	8.59 ± 0.39

[a]The hydrogen atoms of C_{13} have not been considered since this carbon atom is too far from the hydrogen acceptor oxygen atom to undergo any hydrogen abstraction.

3.4. QM/MM Calculations. For clarity, the set of reactions we have studied in this paper are shown in Figure 4. Two successive processes take place to convert AA into LTA_4: hydroperoxidation of AA leading to 5(*S*)-HpETE and epoxidation of this intermediate to finally form LTA_4. The corresponding QM/MM results for each step will be discussed in this section.

3.4.1. Hydroperoxidation of AA. The different reaction steps that lead to the hydroperoxidation of AA by human-5-LOX will be described in the following subsections.

3.4.1.1. Abstraction of H_{7proS} from C_7 of AA. As explained above, three precatalytic structures of the MD simulation (snapshots 914, 15,204, and 19,833) of the h-5-LOX:AA Michaelis complex have been randomly chosen to perform the hydrogen abstraction from C_7. For each structure, the hydrogen atom of C_7 that was closest to the acceptor oxygen atom of the Fe(III)−OH^- cofactor was selected to be abstracted. This hydrogen atom is always H_{7proS}, which is also well orientated due to the applied filter. Taking as a starting point the optimized geometry corresponding to each selected precatalytic structure, the corresponding potential energy profile has been calculated as a function of the reaction coordinate (Figure S6). This reaction coordinate has been defined as the difference between the length of the bond that breaks (C_7−H_{7proS}) and the length of the bond that is formed (H_{7proS}−O). As example, panels A, B, and C in Figure 5 show

https://doi.org/10.1021/acscatal.3c04954
ACS Catal. 2024, 14, 637−656

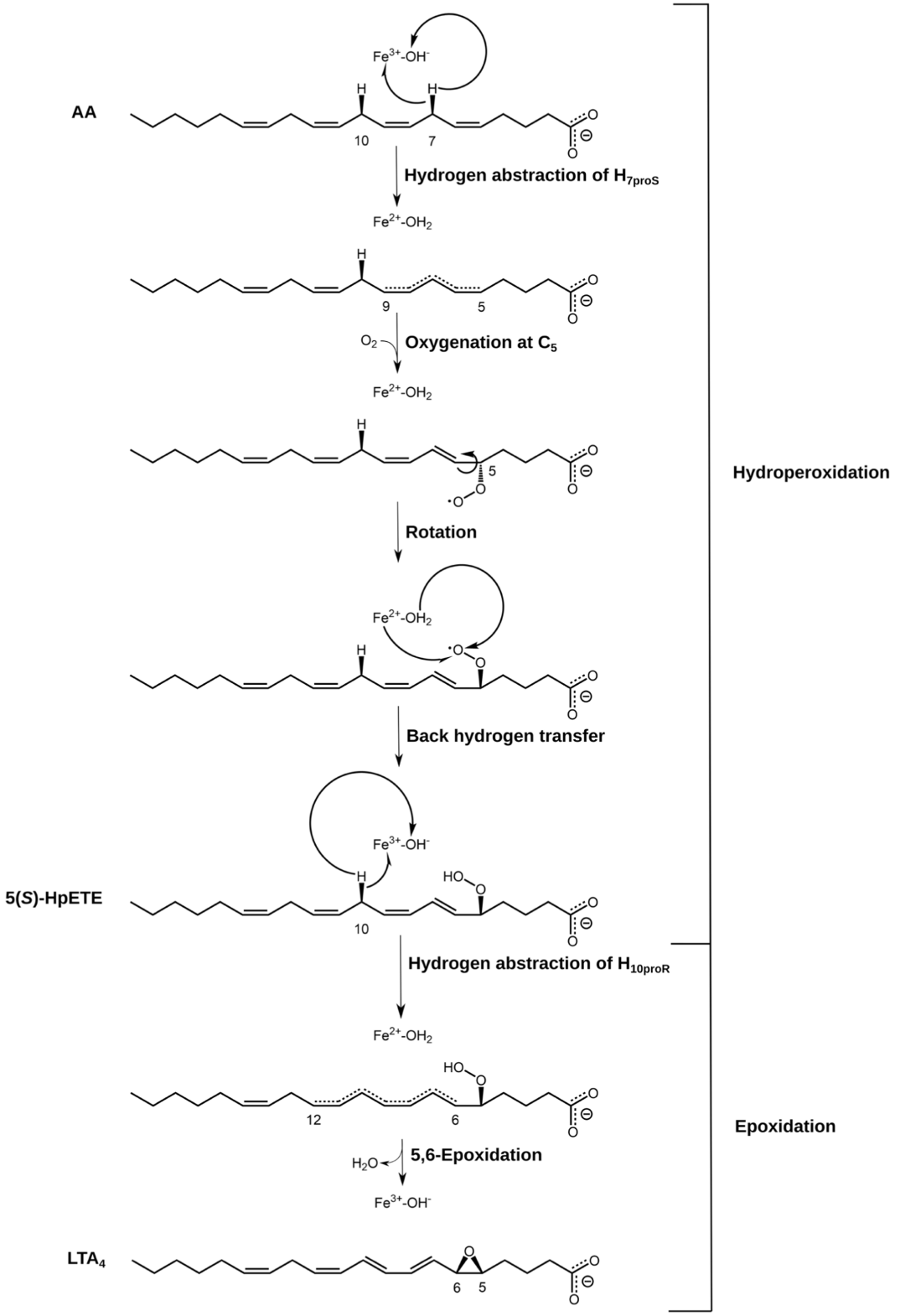

Figure 4. Tentative reaction mechanism of the successive hydroperoxidation and epoxidation processes catalyzed by human-5-LOX when AA acts as a substrate. The hydroperoxidation process develops after the initial abstraction of H_{7proS} from C_7 generating 5(*S*)-HpETE as a product, while the epoxidation process develops after the abstraction of H_{10proR} from C_{10} generating LTA_4 as a final product.

the structures of snapshot 15,204 for reactant, TS, and product, respectively. The resulting potential energy barriers for the three precatalytic structures chosen ranged from 23.3 to 30.3 kcal/mol (Table 3), so exhibiting the usual large dispersion of many enzyme reactions.

The hydrogen abstraction takes places at C_7, placed in the middle of a 1,4-*Z*,*Z*-pentadiene unit, and tends to give rise to a planar system of five electrons delocalized over the five carbon atoms (C_5−C_9) of a π-pentadienyl radical. Thus, the reaction process is quite exoergic (in the least case −10.9 kcal/mol). As

https://doi.org/10.1021/acscatal.3c04954
ACS Catal. 2024, 14, 637−656

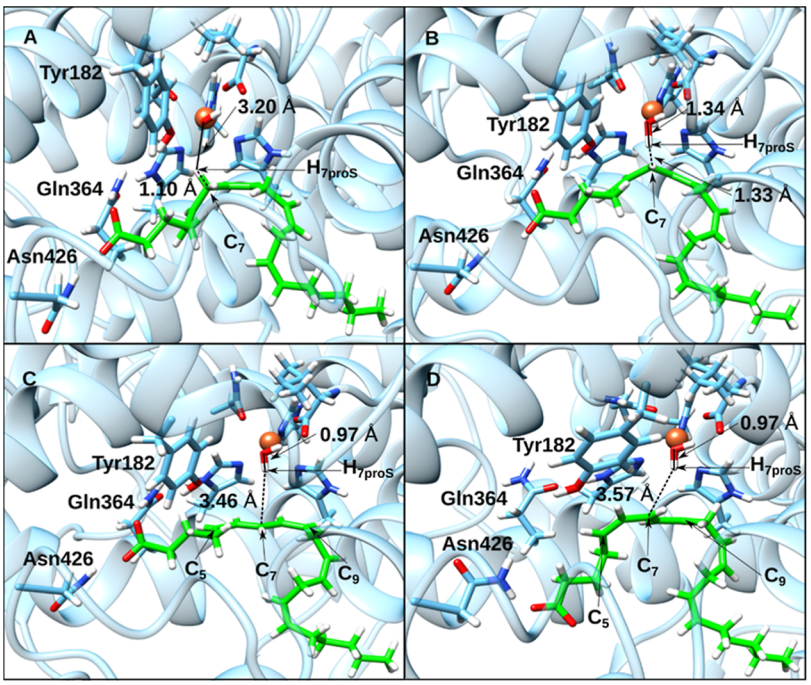

Figure 5. Reactant, TS, and product structures for the H_{7proS} abstraction in snapshot 15,204 (panels A−C, respectively), and product structure for H_{7proS} abstraction in snapshot 914 (panel D).

Table 3. Potential Energy Barriers and Reaction Energies for the H_{7proS} Abstraction in the Different Selected Snapshots

snapshot	$\Delta E^{\ddagger}$ (kcal/mol)	reaction energy (kcal/mol)
914	30.3	−10.9
15,204	23.3	−12.7
19,833	27.4	−15.8

a matter of fact, the abstraction products corresponding to snapshots 15,204 and 19,833 are quite planar, while, as seen in Figure 5, the abstraction product of snapshot 914 slightly deviates from a flat delocalized π-pentadienyl radical. This is the reason why the potential energy profile of snapshot 914 is the least exoergic. Finally, it is interesting to realize that the values obtained for the potential energy barriers corresponding to the abstraction of H_{7proS} of C_7 catalyzed by human-5-LOX are significantly higher than the exponential average potential energy barrier of 19.6 kcal/mol, calculated for the abstraction of H_{13proS} of C_{13} catalyzed by rabbit 15-LOX-1 for the same substrate,[57] which is in agreement with the experimental kinetic data.[72]

3.4.1.2. Oxygenation at C_5 of the π-Pentadienyl Radical. Search for oxygen molecule access channels: A previous step necessary for the study of the addition of the oxygen molecule to the π-pentadienyl radical obtained after the abstraction of H_{7proS} of AA is to determine the channels[73,74] through which the oxygen molecule can access from the protein surface into the active center of the human-5-LOX. These channels have been calculated for the product of the abstraction step of H_{7proS} corresponding to snapshot 15,204, which involves the lowest potential energy barrier for this process among the precatalytic structures studied and is a π-pentadienyl radical totally flat where there is electronic delocalization between C_5 and C_9 (see Figure 5). The calculated channels have been grouped into two clusters (Figure 6). The innermost portion with

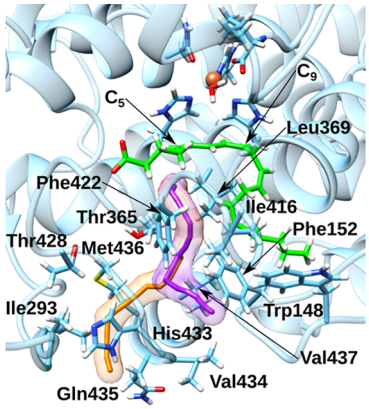

Figure 6. Representation of the two clusters of channels obtained (the best cluster is indicated in violet, while the second-best one is pictured in orange) from the calculated tunnels for an oxygen molecule access into the active center of human-5-LOX from the surface of the enzyme. The main residues defining the tunnels of these clusters, and the C_5 and C_9 carbon atoms of AA have been indicated. Both clusters lead exclusively to C_5.

respect to the surface of the enzyme of the representative tunnels for both clusters coincides. Therefore, there would be two clusters of oxygen channels to the interior of the protein not equivalent to each other, whose paths converge when they approach the cavity where the substrate is bound. It should be noted that the two clusters of channels lead exclusively to C_5, although in principle, the addition of the oxygen molecule could have taken place on either C_5 or C_9. In addition, the diameter of the representative tunnel of both clusters narrows as it approaches the active center of the enzyme. In fact, in the most superficial area of both representative tunnels, the diameter is sufficient to accommodate both the oxygen molecule to be added and various water molecules. The tunnels of the best cluster are defined by the side chains of

https://doi.org/10.1021/acscatal.3c04954
ACS Catal. 2024, 14, 637−656

Trp148, Phe152, Thr365, Leu369, Ile416, Phe422, and Val437, along with the hydrophobic end of AA. The tunnels of the second-best cluster are defined by the side chains of Phe152, Ile293, Thr365, Leu369, Phe422, Thr428, His433, Val434, Gln435, Met436, and Val437. A significant proportion of residues coincides for both clusters of channels since they share their innermost portion with respect to the surface of the enzyme, as mentioned above.

Addition of the oxygen molecule to C_5: The best oxygen channel cluster found above (see Figure 6) for an oxygen molecule attack onto the H_{7proS} abstraction product of snapshot 15,204 has been used to study the oxygen addition. Only oxygenation at C_5 has been considered since the two clusters of channels obtained lead exclusively to that carbon atom. The oxygen molecule was initially placed at about 6.5 Å from C_5. The system was fully optimized at the QM/MM level, only keeping fixed the distance between the nearest oxygen atom of the incoming oxygen molecule and C_5 [d(C_5–O)]. This optimized structure has been used as a starting point to build the potential energy profile for the attack of the oxygen molecule, in which d(C_5–O) has been used as a reaction coordinate. It is important to note that the addition of the oxygen molecule to C_5 occurs antarafacially with respect to the Fe(II)–OH_2 cofactor (Figure 7), giving rise to a peroxide

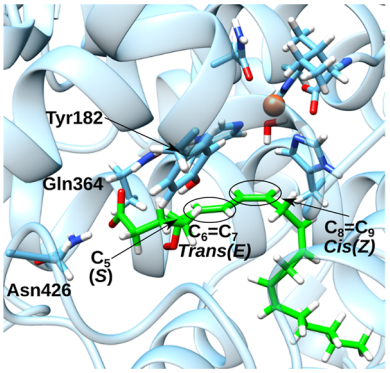

Figure 7. Peroxide radical corresponding to the addition of an oxygen molecule at C_5 of the H_{7proS} abstraction product of snapshot 15,204.

radical that exhibits a stereochemistry compatible with the experimental structure of 5(*S*)-HpETE [that is, the double-bond C_6=C_7 is *trans* (*E*), but C_8=C_9 is *cis* (*Z*), and a configuration *S* at C_5]. The oxygen molecule penetrates the channel without any potential energy barrier until it reaches a minimum energy structure that has been optimized, giving the peroxide radical [d(C_5–O) = 1.50 Å] shown in Figure 7. It is worth emphasizing that this oxygenation is highly exoergic (−38.8 kcal/mol).

3.4.1.3. Rotation of the Peroxide Radical Group at C_5. To form 5(*S*)-HpETE after the addition of the oxygen molecule to C_5, a back-hydrogen transfer to the peroxide radical to form the corresponding hydroperoxide is required. However, the oxygen molecule attacks the π-pentadienyl radical in C_5 antarafacially with respect to the Fe atom, and then, a rotation of one of the C–C bonds containing the peroxide group is necessary to achieve a suprafacial arrangement and make the back-hydrogen transfer possible, which would come from the Fe(II)–OH_2 cofactor of the enzyme.

The optimized peroxide radical product (Figure 7) has been selected as the starting point to start that rotation. The reaction coordinate to reach a suprafacial arrangement of the peroxide radical was defined as a rotation around one of the C–C bonds containing that group. This motion can be described by a dihedral angle centered on the carbon atoms that define the bond around which such rotation takes place. Of the different possible dihedral angles, the dihedral angles < (O_1–**C_5**–C_6–C_7) and < (O_1–**C_5**–C_4–C_3) have been chosen (O_1 stands for the oxygen atom of the peroxide bonded to C_5) since they seem the most suitable to achieve a suprafacial arrangement of the peroxide radical group without involving too high potential energy barriers. In addition, it is possible to define two directions of rotation for each dihedral angle, clockwise and counterclockwise (these directions of rotation are defined by looking at the substrate from its hydrophobic end, see Figure S7). Therefore, there are four possible rotations of dihedral angles to reach this suprafacial arrangement. None of the rotations around < (O_1–**C_5**–C_6–C_7) led to a peroxide suprafacial arrangement, whereas the rest of the AA atoms are those that are rearranged in both directions of that rotation. This result highlights the flexible nature of the substrate. On the other hand, both directions of the rotation around < (O_1–**C_5**–C_4–C_3) take the peroxide group to an almost suprafacial arrangement after a significant reorganization of the carbon atoms C_3, C_4, and C_5 of AA. The clockwise direction leads to the structure shown in Figure S8 (at −59.7°) through a potential energy profile with a smooth curve that involves a potential energy barrier of only 0.7 kcal/mol and a reaction energy of −12.3 kcal/mol. The counterclockwise rotation will not be considered because the subsequent potential energy barriers from its corresponding nearly suprafacial structure are higher than in the case of the clockwise rotation.

From the structure shown in Figure S8, the rotation of the < (O_2–O_1–**C_5**–C_6) dihedral angle has been performed to properly orient the oxygen atom (O_2) of the peroxide radical that must receive the hydrogen atom from the Fe(II)–OH_2 cofactor. As before, this rotation can be done in two directions, clockwise and counterclockwise (these directions of rotation are defined by looking at the substrate in the direction of the C_5–O_1 bond, leaving O_1 ahead of C_5, Figure S9). Both directions of rotation manage to orient the O_2 atom toward the Fe(II)–OH_2 cofactor. In addition, both directions exhibit a potential energy profile with a smooth curve and a remarkably small potential energy barrier (3.6 and 0.4 kcal/mol for counterclockwise and clockwise rotations, respectively). Only the product of the counterclockwise rotation is shown (Figure 8) since from it a substantially lower potential energy barrier

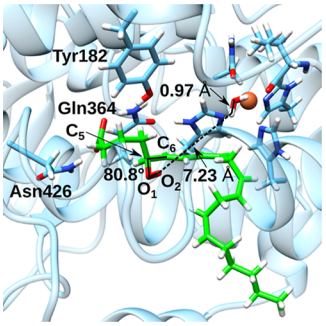

Figure 8. Product structure corresponding to the counterclockwise rotation around the < (O_2–O_1–**C_5**–C_6) dihedral angle. The oxygen atom (O_2) of the peroxide radical that must undergo the back-hydrogen transfer is well oriented toward the Fe(II)–OH_2 cofactor. The distances of interest have also been indicated.

https://doi.org/10.1021/acscatal.3c04954
ACS Catal. 2024, 14, 637–656

will be obtained for the subsequent back-hydrogen transfer than for the case of the clockwise rotation. This product appears at 80.8° involving a reaction energy of −1.4 kcal/mol.

3.4.1.4. Back-Hydrogen Transfer to the Peroxide Radical Group at C_5. Once the peroxide radical group has reached a suprafacial arrangement and the outermost oxygen atom of the peroxide is oriented toward the Fe(II)−OH_2 cofactor, that oxygen atom evolves toward one of the hydrogen atoms of the cofactor, so that the back-hydrogen transfer takes place. The difference between the length of the bond that breaks (O−H of OH_2 of the cofactor) and the length of the bond that is formed (O−H of the resulting hydroperoxide group) has been chosen as a reaction coordinate. The optimized product structure corresponding to the counterclockwise rotation around the < (O_2−O_1−C_5−C_6) dihedral angle (Figure 8) has been taken as the starting point for this reaction profile. This process involves two steps with two potential energy barriers. The first step corresponds to the peroxide radical group adopting a totally suprafacial arrangement, in such a way that its outermost oxygen atom (O_2) becomes close enough to the hydrogen atom of the Fe(II)−OH_2 cofactor that will be back-transferred (see TS and product in panels A and B, respectively, of Figure 9). This step involves a potential energy

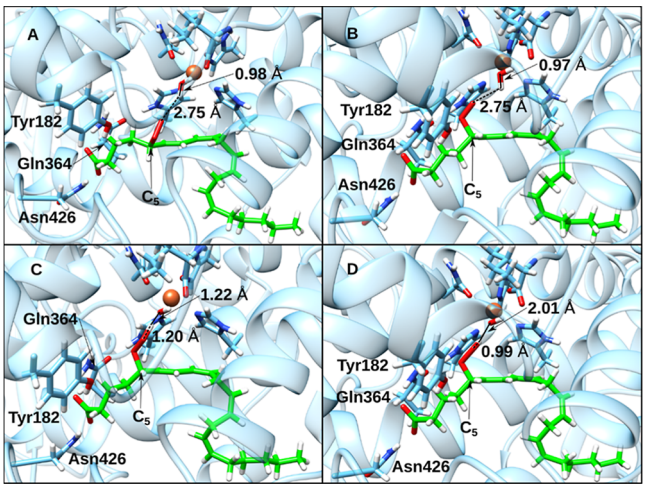

Figure 9. TS and product structures for the two steps corresponding to the back-hydrogen transfer to the peroxide radical group at C_5. Panels A and B correspond to the first step (TS structure and product, respectively), while panels C and D correspond to the second step (TS structure and product, respectively). 5(*S*)-HpETE has been formed as the final product structure of the back-hydrogen transfer (panel D).

barrier of 22.3 kcal/mol and a reaction energy of 10.4 kcal/mol, with a significant reorganization of the substrate, more specifically, of its first 10 carbon atoms.

On the other hand, the second step corresponds to the back-hydrogen transfer itself. To obtain a smooth enough potential energy profile for this second step employing the same reaction coordinate, the profile has been calculated by performing a forward and backward scan. The final profile involves a potential energy barrier of 20.6 kcal/mol and a reaction energy of 6 kcal/mol (see TS and product in panels C and D, respectively, of Figure 9). As a result of the back-hydrogen transfer, the peroxide radical is reduced to a hydroperoxide group, so generating 5(*S*)-HpETE (panel D of Figure 9), which is the final product of the hydroperoxidation process catalyzed by human-5-LOX, and the Fe(III)−OH^- cofactor has been regenerated to initiate a new catalytic cycle, which should eventually lead to the formation of 5,6-epoxide of LTA_4.

Finally, one could wonder if the formed intermediate 5(*S*)-HpETE remains in a pose that is compatible with the subsequent formation of 5,6-epoxide which leads to the final LTA_4, through the abstraction of H_{10proR} from C_{10} of 5(*S*)-HpETE. To address this issue, a MD simulation of 200 ns for the human-5-LOX:5(*S*)-HpETE Michaelis complex was run. The optimized structure of 5(*S*)-HpETE inside the 5-LOX cavity obtained from the above-described hydroperoxidation of AA was taken as a starting structure for that MD simulation. Analyzing the evolution of the distances from the C_{10} hydrogen atoms (H_{10proS} and H_{10proR}) to the oxygen atom of the Fe(III)−OH^- cofactor throughout the MD simulation (see Figure S10), it can be seen that the H_{10proR} abstraction is preferred over the H_{10proS} one, and not only 5(*S*)-HpETE remains in a pose compatible with the H_{10proR} abstraction, but it also improves its position to undergo this hydrogen abstraction. At this point, it is worth noticing that 5(*S*)-HpETE is capable of reorganizing itself inside the human-5-LOX cavity to favor the H_{10proR} abstraction versus the H_{10proS} (compare with Figure S5B).

3.4.2. Epoxidation of 5(S)-HpETE to Form LTA_4. The different reaction steps that lead to the epoxidation of 5(*S*)-HpETE by human-5-LOX will be described in the following subsections.

3.4.2.1. Abstraction of H_{10proR} from C_{10} of 5(S)-HpETE. The first step of the epoxidation process consists of the abstraction of H_{10proR} from C_{10} of 5(*S*)-HpETE, resulting from the previous hydroperoxidation process, to generate a planar system of seven electrons delocalized over the seven carbon atoms (C_6−C_{12}) of a π-heptatrienyl radical. The starting point to calculate the potential energy profile of this hydrogen abstraction is the structure corresponding to 5(*S*)-HpETE (see panel D of Figure 9). The hydrogen atom at C_{10} of that structure closest to the hydrogen acceptor oxygen atom of the Fe(III)−OH^- cofactor is pro*R*, as suggested by the experimental results.[13] The reaction coordinate has been defined as the difference between the length of the bond that breaks (C_{10}−H_{10proR}) and the length of the bond that is formed (H_{10proR}−O). As in the back-hydrogen transfer case described above, the profile has been calculated by performing a forward and backward scan. The final profile (see Figure S11, whose TS and product are in panels A and B of Figure 10, respectively) is smooth and involves a potential energy barrier of 20.2 kcal/mol and a reaction energy of −16.3 kcal/mol. This

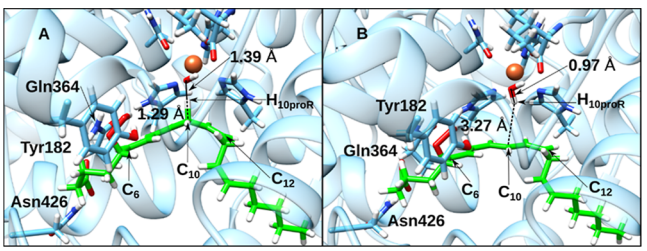

Figure 10. TS (panel A) and product (panel B) structures for the H_{10proR} abstraction from C_{10} of 5(*S*)-HpETE. The planar system of seven electrons delocalized over the seven carbon atoms (C_6−C_{12}) of a π-heptatrienyl radical can be seen in the product structure.

https://doi.org/10.1021/acscatal.3c04954
ACS Catal. 2024, 14, 637−656

reaction turns out to be very exoergic due to the formation of an extended planar system of seven electrons delocalized over the seven carbon atoms (C_6−C_{12}) of a π-heptatrienyl radical. This extended conjugation of the π-radical in the product also contributes to lower the hydrogen abstraction barrier (compare with the above case of the H_{7proS} abstraction where a shorter (C_5−C_9) π-pentadienyl radical was formed).

3.4.2.2. 5,6-Epoxidation. The second and final step of the epoxidation consists in the 5,6-epoxide ring-closure of the 5(*S*)-HpETE π-heptatrienyl radical resulting from the previous H_{10proR} abstraction to form the final LTA_4 product. Two different mechanisms can be envisaged in order to form this epoxide ring:[16] (1) homolytic cleavage of the hydroperoxide group at C_5 along with a hydrogen atom transfer from the Fe(II)−OH_2 cofactor to form a water molecule and the 5,6-epoxide closure by radical recombination and (2) homolytic cleavage of the hydroperoxide group along with an inner sphere electron transfer directly from the iron atom of the Fe(II)−OH_2 cofactor.

As explained in the Supporting Information [see the section entitled 5,6-epoxide ring-closure of the 5(*S*)-HpETE π-heptatrienyl radical following a hydrogen atom transfer from the Fe(II)−OH_2 cofactor], the first mechanism based on the hydrogen atom transfer can be discarded because it does not lead to the formation of the 5,6-epoxide and, therefore, to the formation of LTA_4. With the aim of exploring the second mechanism, three different reaction coordinates had to be successively used. Initially, a linear combination of three bond lengths, specifically d(O_{inner}−O_{outer}) − d(O_{outer}−Fe) − d(O_{inner}−C_6), was employed in order to move closer O_{outer} to the iron atom of the Fe(II)−OH_2 cofactor, while at the same time it is favoring the cleavage of the peroxide bond and the formation of the 5,6-epoxide (O_{inner} and O_{outer} make reference to the hydroperoxide oxygen atoms, being O_{inner} the one directly attached to C_5). The optimized geometry of the product of the H_{10proR} abstraction from 5(*S*)-HpETE (see Figure 10B) was employed as a starting point to construct the corresponding potential energy profile. Next, a rotation around the < (C_6−C_7−C_8−C_9) dihedral angle was used as a reaction coordinate with the objective of breaking the planarity of the π-heptatrienyl radical (C_6−C_{12}). This rotation favors the 5,6-epoxide ring-closure because the steric hindrance for closing this ring due to the hydrogen atom attached to C_6 is reduced, and O_{outer} is better positioned to be transferred later to the iron atom of the Fe(II)−OH_2 cofactor as a hydroxide anion (compare panels C and D of Figure 11). For each possible rotation direction of that dihedral angle, clockwise and counterclockwise (these rotation directions are defined looking at the substrate from the carboxylate side, see panel C of Figure 11), a potential energy profile was calculated, being the clockwise rotation the one with the smaller potential energy barrier. Both potential energy profiles were constructed starting from the optimized geometry associated with the third minimum (panel C of Figure 11) obtained using the initial reaction coordinate. For the sake of brevity, only the results concerning to the clockwise rotation will be exposed. Finally, with the aim of forming the 5,6-epoxide and provoking the inner sphere electron transfer, the length of the nascent bond O_{inner}−C_6 was chosen as the third reaction coordinate. The product of the clockwise rotation of the < (C_6−C_7−C_8−C_9) dihedral angle was chosen as starting point to calculate this last potential energy profile (panel D of Figure 11).

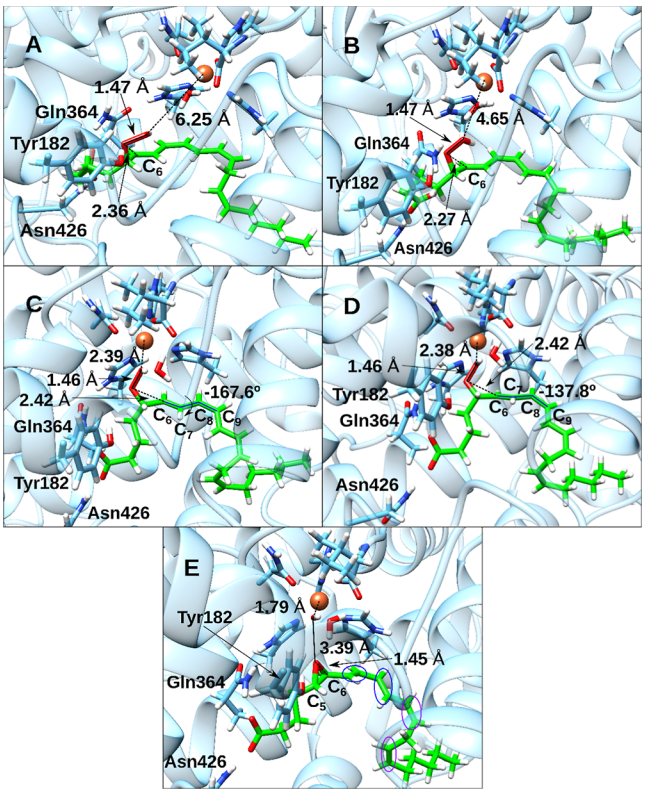

Figure 11. Successive five minimum energy structures (A to E, see text) corresponding to the products along the three reaction coordinates associated with the mechanism based on an inner sphere electron transfer to form the 5,6-epoxide. Panels C and D show how the clockwise rotation of the < (C_6−C_7−C_8−C_9) dihedral angle breaks the planarity of the π-heptatrienyl radical, so favoring the 5,6-epoxide ring-closure. It is important to note that panel E corresponds to the optimized geometry of LTA_4, whose *Z* and *E* double bonds have been encircled in purple and blue colors, respectively.

The potential energy profile corresponding to the first reaction coordinate shows three feasible potential energy barriers whose values are 16.3, 19.7, and 17.0 kcal/mol, respectively. Initially, along the first potential energy barrier, the outer oxygen atom of the hydroperoxide group at C_5 gets closer to the iron atom of the Fe(II)−OH_2 cofactor [d(Fe−O_{outer}) evolves from 7.91 to 6.25 Å], the hydrogen bond between O_{outer} and the OH group of Tyr182 is weakened [d(O_{outer}−HO−Tyr182) evolves from 1.73 to 2.56 Å], and a new one is formed between the same protein residue and the other oxygen atom of the hydroperoxide group [d(O_{inner}−HO−Tyr182) evolves from 2.38 to 2.20 Å]. Additionally, Leu608 leaves its position, what makes easier the approach between the hydroperoxide group and the Fe(II)−OH_2 cofactor. However, the breaking O−O bond of the hydroperoxide at C_5, the nascent O_{inner}−C_6 bond and the Fe(II)−OH_2 cofactor do not suffer significant changes. This first step is endoergic, and its product (panel A of Figure 11) is 8.9 kcal/mol above the starting structure (Figure 10B). On the other hand, during the second potential energy barrier, O_{outer} continues getting closer to the iron atom of the Fe(II)−OH_2 cofactor [d(Fe−O_{outer}) = 4.65 Å]. Moreover, in order to adjust to this approach the following two processes take place: (1) the substrate suffers an important reorganization placing its tail deeper into the cavity bottom, which allows that the hydroperoxide group at C_5 gets closer to the iron atom of

https://doi.org/10.1021/acscatal.3c04954
ACS Catal. 2024, 14, 637−656

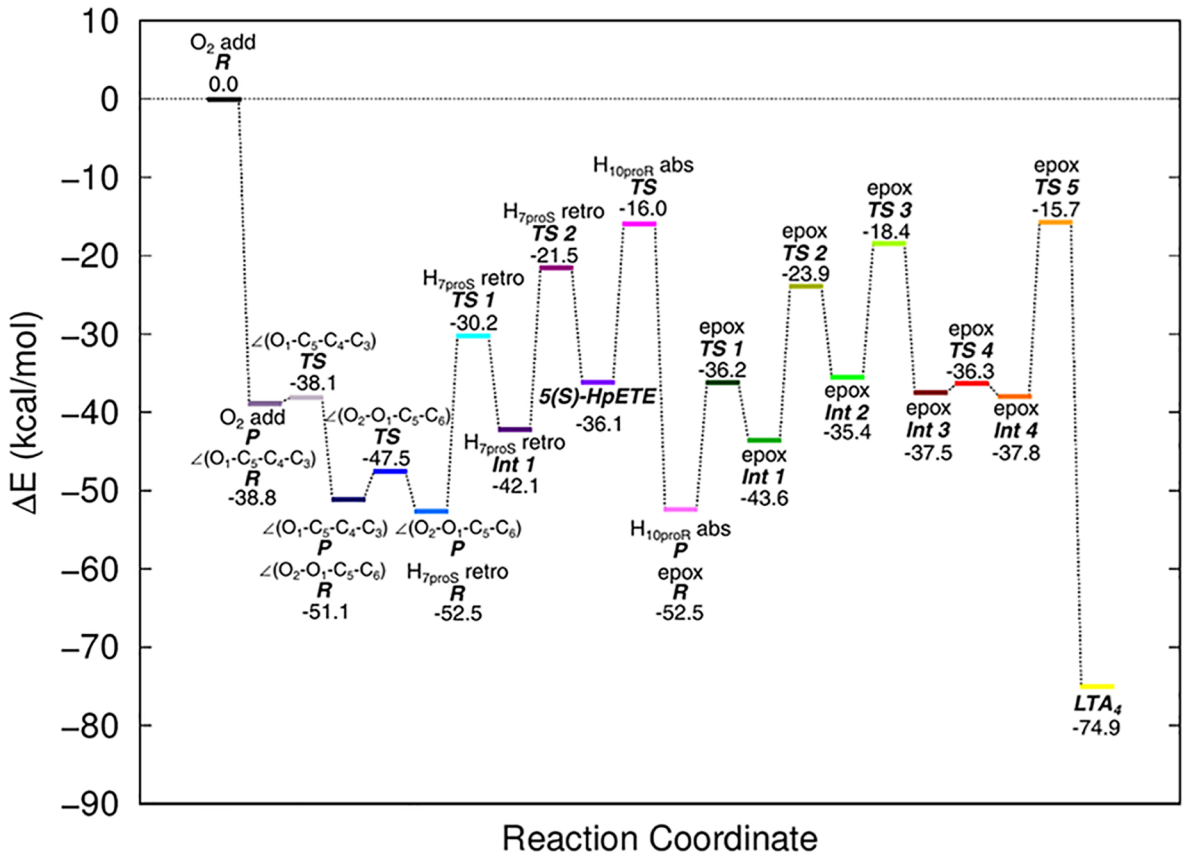

Figure 12. Overall energy scheme including the addition of the oxygen molecule to C_5, the two rotations of the peroxide radical group at C_5, the two steps corresponding to the back-hydrogen transfer to the peroxide radical group at C_5, the H_{10proR} abstraction, and the five steps corresponding to the epoxidation of 5(*S*)-HpETE to form LTA_4. All energies are in kcal/mol. The zero of energies corresponds to the product of the H_{7proS} abstraction step bound to the solvated enzyme plus an oxygen molecule within the water box whose position has been optimized at 6.5 Å from the C_5 atom of the substrate.

the Fe(II)−OH_2 cofactor without losing the planarity of the π-heptatrienyl radical from C_6 to C_{12}; (2) the water molecule of the Fe(II)−OH_2 cofactor slightly moves away from its position getting closer to the terminal Ile674, and leaving some room for the incoming hydroperoxide group. This second step is also endoergic, and its product (panel B of Figure 11) is 8.2 kcal/mol above the product of the previous step. Finally, the third potential energy barrier is associated with the close approach, although not yet transfer, of the O_{outer} atom to the iron atom of the Fe(II)−OH_2 cofactor and the departure of the water molecule. The optimized geometry of the product (panel C of Figure 11) corresponding to this third barrier shows the following main features: (1) O_{outer} is faced toward the iron atom and both are close enough to each other [d(Fe−O_{outer}) = 2.39 Å] to allow the homolytic cleavage of the hydroperoxide group along with an inner sphere electron transfer from the iron atom; (2) the planarity of the π-heptatrienyl radical between C_6 and C_{12} is preserved; (3) the released water molecule forms a water bridge that connects O_{outer} with the terminal residue Ile674; and (4) the breaking O−O bond of the hydroperoxide at C_5 and the nascent O_{inner}−C_6 bond do not suffer any significant changes in comparison with the starting structure of this reaction coordinate [d(O_{inner}−C_6) = 2.42 Å; d(O_{inner}−O_{outer}) = 1.46 Å]. Unlike the two previous steps, this third step is exoergic, and its product is 2.2 kcal/mol below the product of the previous step. From this point, if this reaction coordinate is continued, upon overcoming a potential energy barrier of 23.1 kcal/mol, which would be the highest one considering all potential energy barriers of this second mechanism, the cleavage of the O−O bond and the transfer of the hydroxide anion to the iron atom takes place; however, the 5,6-epoxide formation would not be achieved yet. For this reason, the subsequent reaction coordinates are necessary to form the 5,6-epoxide.

The potential energy profile associated with the second reaction coordinate is quite simpler, since it only contains a small potential energy barrier of 1.2 kcal/mol. In the obtained product (panel D of Figure 11), which is localized at < (C_6−C_7−C_8−C_9) = −137.8°, the planar system corresponding to the π-heptatrienyl radical from C_6 to C_{12} is broken without significantly altering the lengths of the breaking O−O bond of the hydroperoxide at C_5 and the nascent O_{inner}−C_6 bond. This dihedral rotation is slightly exoergic, with a reaction energy of −0.3 kcal/mol.

At this point, everything is ready for the inner sphere electron transfer to occur directly from the Fe atom, so synchronically triggering the homolytic cleavage of the hydroperoxide, the hydroxide anion transfer to the iron atom, and the formation of the O_{inner}−C_6 epoxide bond. All those chemical changes take place along the potential energy profile associated with the third reaction coordinate, which only presents a potential energy barrier of 22.1 kcal/mol, that corresponds to the 5,6-epoxide formation itself. The optimized structure of the obtained product with this reaction coordinate

https://doi.org/10.1021/acscatal.3c04954
ACS Catal. 2024, 14, 637−656

is finally LTA_4, with the appropriate stereochemistry for the double bonds and the epoxide (double bonds C_7-C_8 and C_9-C_{10} show an *E* stereochemistry, double bonds $C_{11}-C_{12}$ and $C_{14}-C_{15}$ exhibit a *Z* stereochemistry, and both carbon atoms involved in the 5,6-epoxide show a *S* configuration, see panel E of Figure 11). This epoxide ring-closure is exoergic, with a reaction energy of −37.1 kcal/mol with respect to the product of the previous step (Int 4). Thus, the homolytic cleavage of the hydroperoxide group along with an inner sphere electron transfer directly from the iron atom of the $Fe(II)-OH_2$ cofactor seems the suitable mechanism for the 5,6-epoxide formation.

To summarize the different QM/MM steps, the overall energy scheme starting from the product of the H_{7proS} abstraction step bound to the solvated enzyme plus an oxygen molecule within the water box whose position has been optimized at 6.5 Å from the C_5 atom of the π-pentadienyl radical is displayed in Figure 12. This structure has been taken as the zero of energy of the overall energy scheme. The addition of the oxygen molecule to C_5 involves a falloff in potential energy of 38.8 kcal/mol with respect to the H_{7proS} abstraction product. This lost potential energy is transformed to kinetic energy, which is in part dissipated among nonreactive vibrational modes, and partially employed to provide enough energy to surmount the energy barriers for the following reaction steps, given that these energy barriers for the two rotations of the peroxide radical group at C_5, the two steps corresponding to the back-hydrogen transfer to the peroxide radical group at C_5, the H_{10proR} abstraction, and the five steps corresponding to the epoxidation of 5(*S*)-HpETE to form LTA_4 appear very far below the reference structure. Therefore, none of those processes, but the H_{7proS} abstraction from C_7 of AA (see Table 3 and Figure S6), can be the rate-determining step of the LTA_4 formation reaction.

3.5. Arachidonic Acid Active Site Access. Once the reaction mechanisms of the two successive processes [hydroperoxidation of AA and epoxidation of 5(*S*)-HpETE] that convert AA into LTA_4 catalyzed by the enzyme human-5-LOX have been studied, our focus will be addressed to discuss the intriguing topic of how AA gains access to the active site of human-5-LOX to undergo that transformation.

CAVER 3.0 was used to analyze the MD simulation of the human-5-LOX:AA Michaelis complex with the aim of determining possible channels connecting the bulk solvent with the human-5-LOX active site, which can be employed by AA to enter this cavity. For this purpose, 40 evenly spaced structures were selected from this MD simulation. Although a great deal of channels has been obtained, three main channels (see Figure 13) can be identified. Two of them flow toward the AA ends, in particular, channel A, which involves Trp148, leads to the AA carboxylate group, while channel C leads to the AA tail. In contrast, channel B flows toward the central part of AA and involves residues Phe178 and Tyr182. It is important to note that channels A and B had been already proposed.[19] With the aim of studying the role of these three main channels, a representative set of structures was selected for each one with the channel open, since they are not always open along the MD trajectory. Additionally, every main channel has its own frequency of appearance which resulted in a different number of structures for each representative set (see Table 4). According to the CAVER 3.0 parameter to assess the suitability of channels, called as priority, channel A would be the most probable route for AA to enter and leave the human-5-LOX active site since it has the highest value. Additionally, channel B should be a slightly better route in comparison to channel C.

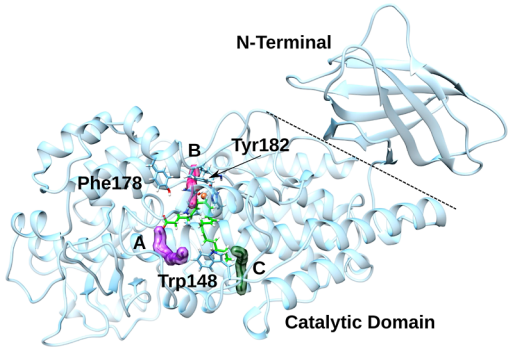

Figure 13. Representation of three main channels connecting the bulk solvent with the human-5-LOX cavity. Two of them flow toward the AA ends (channel A leads to the AA carboxylate group, while channel C leads to the AA tail), whereas channel B flows toward the central region of AA. The channel A involves Trp148 and the channel B implicates Phe178 and Tyr182. AA is depicted in green.

Table 4. Priority and Number of Structures of the Corresponding Representative Set for the Three Main Channels Obtained[a]

channel	number of structures of the representative set	priority
A	31	0.677
B	41	0.487
C	20	0.406

[a]For each channel, the value of the priority parameter corresponds to the average over the structures of its representative set.

On the other hand, to study how AA can enter and leave the human-5-LOX cavity through these three main channels, a SMD simulation for each structure of the different representative sets was carried out. For each representative set, a proper coordinate to extract AA along its SMD simulations was used: (1) channel A: $d(C_1-C_\alpha$-Asn555); (2) channel B: $d(C_1-C_\alpha$-Thr428) + $d(C_1-C_\alpha$-Leu369); and (3) channel C: $d(C_{20}-C_\alpha$-Ala425). For avoiding problems of sampling, the cumulant expansion was used to calculate the PMF associated with each channel.

As for channel C, which would imply a head-first entrance of AA into the human-5-LOX cavity, 20 SMD simulations were calculated. In all of them, a loop belonging to the broken helix $\alpha 2$ (residues 143−160) must be displaced to allow AA to leave the human-5-LOX cavity. However, this displacement does not take place in the same way in all cases, giving rise to a bifurcation of the original channel. In fact, the SMD simulations of channel C can be classified according to the side of this loop by which AA leaves the protein cavity. It can be noted that AA is mostly extracted by the right side of this loop (16 over 20 SMD simulations), although the left-side extractions involve an external work much smaller ($\langle W\rangle_{right}$ = 200.31 kcal/mol versus $\langle W\rangle_{left}$ = 141.16 kcal/mol). This result shows that the left-side AA extractions are easier, but structures capable of undergoing this extraction are less frequent. On the other hand, the average forces that should be applied to achieve the AA extractions by both sides of channel C (see panels A and B of Figure 14) are quite large, which agrees with the relatively high external works obtained. Regarding the calculated PMFs, for right-side extractions (see panel D of Figure 14), it can be noticed that the channel associated with

https://doi.org/10.1021/acscatal.3c04954
ACS Catal. 2024, 14, 637−656

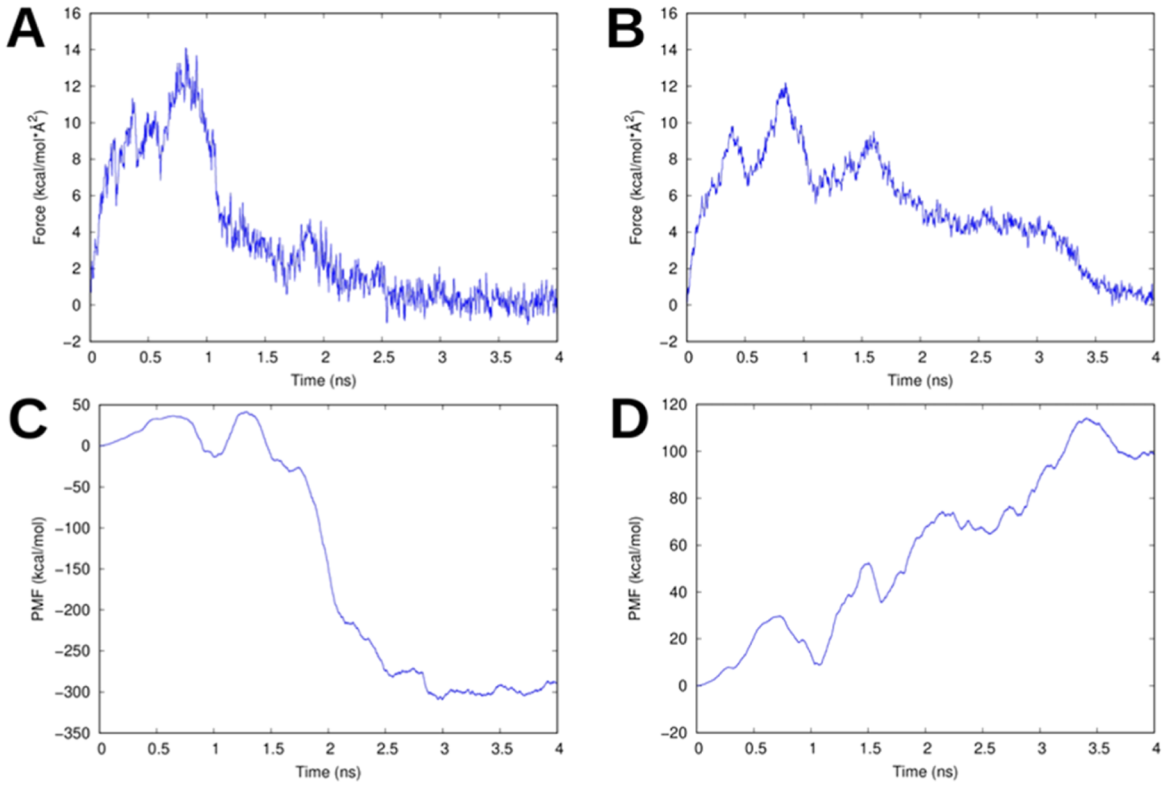

Figure 14. Average forces and PMFs for AA extractions through channel C. Panels A and C correspond to AA extractions which take place on the left side of the broken-helix α2 loop (residues 143−160), while panels B and D correspond to AA extractions which take place on the right side of that loop.

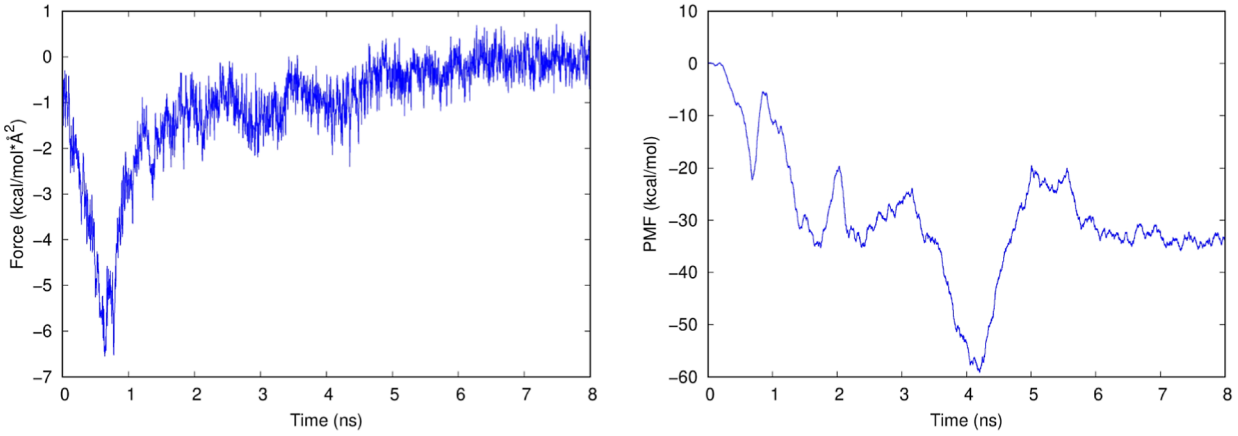

Figure 15. Average forces (left) and PMF (right) for AA extractions through channel B.

them would be only adequate for entering the human-5-LOX active site. However, the resulting system after this extraction has a high energy which is probably associated with unstable protein conformations, since large forces and a high external work were necessary to pull out AA. Considering that these high energy conformations would be barely populated, it can be concluded that the channel for right-side extractions would be in fact ineffective both for AA entering and leaving the human-5-LOX cavity. However, though it is necessary more sampling in order to obtain more accurate values, considering the PMF for left-side extractions (see panel C of Figure 14), it can be concluded that the channel would be inadequate both for AA entering and leaving since the system is much more stable when AA is in the solvent. Although the Gibbs energy barrier to pull out AA from the human-5-LOX cavity through this channel is much smaller than to enter, it is totally unfeasible (around 50 kcal/mol). Therefore, channel C is ineffective both for the AA entrance and AA leaving the human-5-LOX cavity regardless of the side of the broken helix α2 loop which AA employs to leave the protein cavity.

Regarding channel B, which would imply a tail-first entrance of AA into the human-5-LOX cavity, 41 SMD simulations were calculated, of which 35 had to been discarded because either AA left the human-5-LOX cavity using different alternative channels to the considered one, or an excessive external work had to be employed to achieve a complete AA extraction. According to the calculated average forces and the PMF for channel B (Figure 15), AA can abandon the protein cavity in a

https://doi.org/10.1021/acscatal.3c04954
ACS Catal. 2024, 14, 637−656

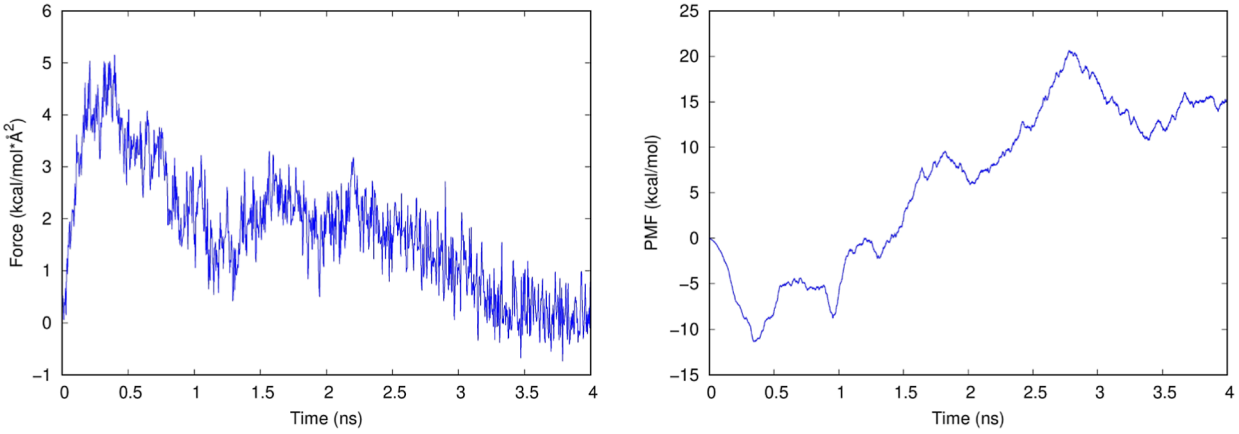

Figure 16. Average forces (left) and PMF (right) for AA extractions through channel A.

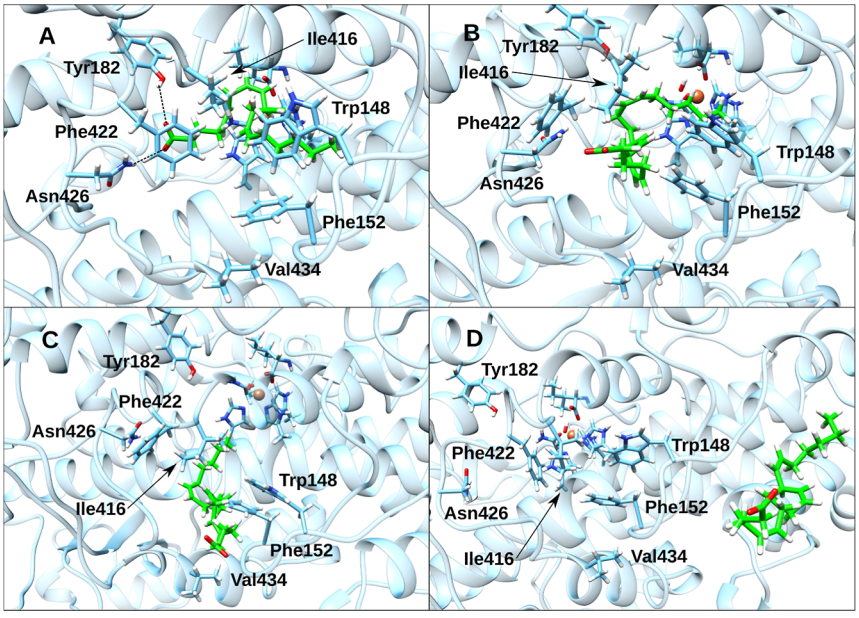

Figure 17. Unbinding process of AA (in green) through channel A. The starting structure (panel A) and the structures of minimum average force associated with the three peaks observed in the force profile (panels B−D represent the minima of peaks at 0.4, 1.55, and 2.25 ns, respectively) have been depicted. Protein residues which either anchor AA to the active site (Tyr182 and Asn426) or constitute the bottleneck of channel A were pointed out.

barrierless way, and the system is much more stable when AA is found in the solvent. In fact, when the system leaves its initial equilibrium position inside the enzyme, it evolves to this state applying very little external work (the external average forces are moderate and mostly negative). Additionally, a very stable intermediate structure exists, and the system stability is almost equal at both sides of it. However, from this intermediate structure, the Gibbs energy barrier to be overcome is larger for leaving the human-5-LOX cavity rather than for entering it (around 5 kcal/mol energy difference). Therefore, though the system has enough energy to reach the state where AA is in the bulk solvent, this would tend to evolve backward instead of forward regarding the extraction of AA into the solvent. Furthermore, considering the time scale in which the departure of AA takes place, some degree of thermalization should occur, which could result in the system being trapped into the minimum associated with this very stable intermediate structure. According to our results, channel B would be inadequate both to AA entry and leaving the human-5-LOX protein cavity due to the existence of this very stable intermediate structure and its backward and forward Gibbs energy barriers.

In relation to channel A, which implies a tail first-entrance of AA into the human-5-LOX active site, 31 SMD simulations were calculated, though five had to been discarded due to the excessive external work that had to be employed for pulling out AA. According to the calculated PMF for channel A (Figure 16), AA can enter the human-5-LOX cavity overcoming a small Gibbs energy barrier (around 8 kcal/mol). However, leaving this cavity is also feasible but implying a significantly larger Gibbs energy barrier (around 21 kcal/mol). Additionally, the system is more stable when AA is found in the human-5-LOX cavity, which agrees with the average forces calculated, since they are mostly positive, though moderate. Figure S13 shows how solvation of AA along its unbinding process changes. It can be seen that AA increases its interaction with water molecules, while it penetrates the bulk solvent (see panels A−D). On the other hand, this smaller interaction with

https://doi.org/10.1021/acscatal.3c04954
ACS Catal. 2024, 14, 637−656

water molecules when AA is found inside the human-5-LOX pocket is compensated with interactions with residues that constitute this pocket. Therefore, taking everything into account, this channel is effective both for AA entering and leaving the protein pocket, although the entrance would be more favorable.

In conclusion, on the basis of our results, for the human-5-LOX in a closed conformation, AA enters and leaves the protein pocket through channel A exclusively. Therefore, it is only worth analyzing the unbinding process of AA from the human-5-LOX cavity through channel A. The force profile for pulling out AA through channel A (left graphic of Figure 16) shows three peaks (at 0.4, 1.55, and 2.25 ns), being the first and third peaks very sharp and smooth, respectively. First, the carboxylic group leads the way toward the pocket entrance, but its hydrogen bonds with Asn426 and Tyr182, which anchor AA to the active site, must be previously broken (see panel A of Figure 17). Additionally, first Phe422 and then Trp148 rotate their side chains to leave room for the outgoing carboxylic group (see panel B of Figure 17). All this together would correspond to the first sharp peak, whose sharpness is because cleavage of favorable interactions, reorganizations, and rotations take place at the same time. Next, the end part of AA (from C_{14} to C_{20}) undergoes a reorganization to accommodate into channel A, which would correspond to the second observed peak (see panel C of Figure 17). Finally, the third smooth peak rises from the completeness of AA extraction to the bulk solvent (see panel D of Figure 17). This final peak is smooth since it involves neither cleavage of favorable interactions nor significant reorganizations.

At this point, there are two main questions still to be addressed. The first one would be how the interaction between this enzyme and its helper protein (FLAP) occurs since it is well-known that human-5-LOX reaches its maximum catalytic activity when it acts accompanied by FLAP, whose main role is to supply AA to human-5-LOX from a phospholipid membrane, and in the presence of Ca^{2+}, which favors the release of AA.[20] On the other hand, when these two proteins act together, both the *N*-terminal domain of human-5-LOX and FLAP should be associated with the membrane and at least one entrance to the human-5-LOX cavity should lie close to the AA site in FLAP. Taking all this into account and according to the calculated channels, the most feasible way of interaction between human-5-LOX and FLAP is by means of the human-5-LOX side in which the helix α2 lies, since the *N*-terminal domain of human-5-LOX would point toward FLAP, and therefore toward the phospholipid membrane, and channel B would lie close to the AA site in FLAP. In fact, this way of binding between these two proteins had already been suggested.[23,75] However, in accordance with its calculated PMF, this channel would be inadequate both for AA entering and leaving the human-5-LOX active site. This apparent contradiction is because both channels and their PMFs were calculated using human-5-LOX structures in a closed conformation, with the helix α2 broken and showing a v-like structure, while the preferred conformation for human-5-LOX when interacting with FLAP and a phospholipid membrane would be the open one,[23] with the helix α2 elongated. To analyze the structure of an open conformation, a Stable-5-LOX whose crystal structure exhibits a helix α2 elongated (PDB code 7TTJ) has been taken as a model.[20] Indeed, quite apart from the helix α2 and to a lesser extend the helix α18, the overall structure of human-5-LOX is preserved regardless of its conformation. Given that these two helixes are only involved in channel B, it is expected that both channel A and channel C remain practically unaffected, which would imply that their PMFs are still valid. On the other hand, despite the fact that side chains of Phe178 and Tyr182, which have been postulated that act as a "cork" that shields the human-5-LOX active site,[19] still remain pointing inward the human-5-LOX cavity, this reorganization of the helix α2 along with the small displacement of the helix α18 would change the orientation and spatial arrangement of channel B, making it much wider than in the closed conformation (see Figure 18). It is highly probable that

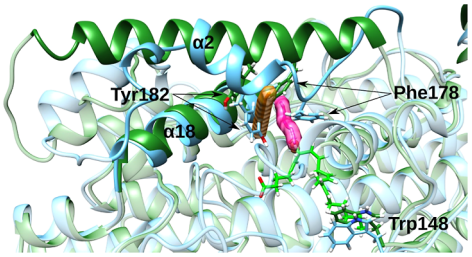

Figure 18. Representation of channel B in the closed and open conformation (fuchsia and orange, respectively). An overlap between both conformations (closed conformation in blue while open one in dark green) has been depicted to stand out the differences between helixes α2 and α18. As a model of open conformation, the structure corresponding to PDB code 7TTJ was used. Phe178 and Tyr182 have been represented to show their alignment in relation with channel B. On the other hand, AA (in green), the Fe(III)−OH^- cofactor and Trp148 have been depicted as a reference point.

this increase in width (see the change of position of Phe178 and Tyr182) associated mainly with the helix α2 elongation favors both entrance and leaving through this new resulting channel. This enlarged width along with the fact that FLAP will only supply AA to this channel make channel B the most suitable one for entering and leaving the human-5-LOX cavity in the presence of FLAP and the phospholipid membrane.

On the other hand, the second question to be addressed is which AA end enters first the human-5-LOX cavity and which would be the resulting alignment of AA in this protein pocket. According to our results, AA can only gain access to the human-5-LOX cavity by means of channels A (closed conformation) or B (open conformation). In both cases, the alignment of AA corresponds to a head-first positioning in the active site,[23] and AA would first introduce its methyl end into the human-5-LOX cavity. This way of entering AA into the human-5-LOX active site is quite clear for channel A (otherwise, AA could not reach a head-first positioning). In turn, a head-first entry for channel B is not possible since would imply a substrate reorganization to place the methyl end of AA and its 1,4-*Z*,*Z*-pentadiene unit centered at C_7 properly to undergo the initial H_{7proS} abstraction. This process would involve a major reorganization of the central part of AA, whose flexibility is reduced due to the presence of double bonds, and therefore, it would be unfavorable with a large Gibbs energy barrier. An important conclusion that can be drawn from these results is that it does not exist a direct relationship between the final alignment of AA in the active site and the AA end which enter the protein pocket first.

Finally, it is important to underline the significant role of Trp148 in channel A. Although Trp148 is one of the bulkiest protein residues, its double-ring polar side chain favors the

https://doi.org/10.1021/acscatal.3c04954
ACS Catal. 2024, 14, 637−656

opening of channel A because it can establish a $\pi-\pi$ stacking interaction with Phe152 and a NH$-\pi$ interaction with Arg412 when this channel is open (panel C of Figures 19 and S14).

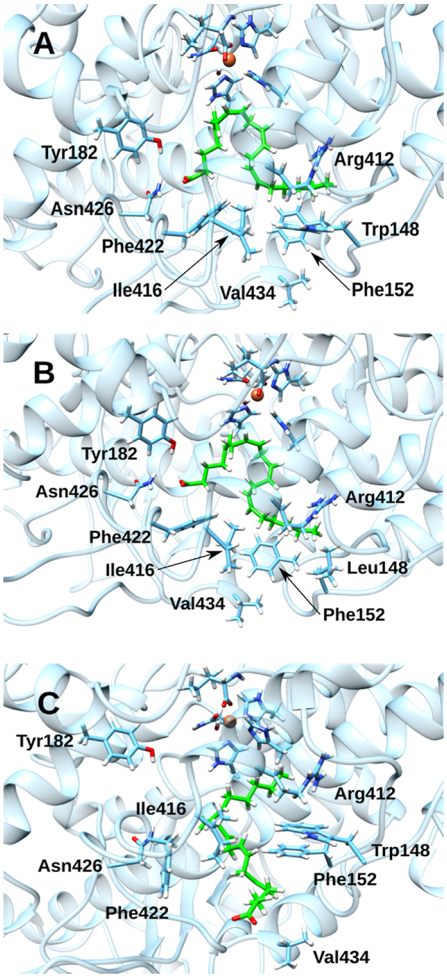

Figure 19. Role of Trp148 in the entrance and leaving of AA (in green) and in the AA binding to the active site. Panels A and C show the placement of Trp148 when channel A is closed or open, respectively. In contrast, panel B shows the placement of Trp148 when it is mutated by Leu148, and channel A is closed. Note that AA has been set inside the cavity by docking in panels A and B, but it cannot enter or leave the enzyme active site through the closed channel A.

However, both favorable polar interactions are lost when channel A is closed (see panel A of Figure 19). On the other hand, if Trp148, with its flat side chain, was mutated to a residue with a less bulky but neither flat nor aromatic side chain, like Leu148, the absence of the $\pi-\pi$ stacking interaction with Phe152 would push this residue to occupy the region of channel A and closing it (panel B of Figure 19). All this would decrease the reactivity of AA, what is supported by the experimental data associated with the Trp148Leu mutation[21] since they show a significant reduction of the catalytic enzyme activity.

4. CONCLUSIONS

The enzyme 5-LOX occupies an exceptional central position in the development of inflammation-based diseases. On the one hand, 5-LOX catalyzes the transformation of AA into LTs, which are potent chemotactic mediators with key pro-inflammatory functions that trigger acute inflammations. On the other hand, 5-LOX also intervenes in the production of lipoxins, which are anti-inflammatory SPMs that promote resolution of the inflammation, so avoiding a chronic inflammatory condition. That is why enormous efforts have been devoted for decades to the discovery of 5-LOX inhibitors that suppress the formation of LTs without decreasing the generation of lipoxins. The lack of a crystal structure for 5-LOX has made this challenging objective very difficult so far. The recent AlphaFold protein structure database prediction of the tridimensional structure of human-5-LOX has enabled us to present here the first available model of the human-5-LOX:AA Michaelis complex. Then, we have combined MD simulations, quantum mechanics/molecular mechanics calculations, and SMD simulations to unravel step by step the molecular mechanism by means of which human-5-LOX converts AA into LTA_4 in the absence of the membrane-embedded FLAP in vitro.

AA presents a stable head-first alignment in the active site of human-5-LOX. The exoergic abstraction of H_{7proS} from C_7 of AA gives rise to a planar system of five electrons delocalized over the five carbon atoms (C_5-C_9) of a π-pentadienyl radical and initiates the hydroperoxidation of AA, then leading to 5(S)-HpETE. This intermediate is retained enough time inside the 5-LOX cavity to allow the very exoergic abstraction of H_{10proR} from C_{10} of 5(S)-HpETE to give an extended planar system of seven electrons delocalized over the seven carbon atoms (C_6-C_{12}) of a π-heptatrienyl radical, thus beginning the epoxidation process that finally leads to LTA_4. The final 5,6-epoxide formation takes place by means of the homolytic cleavage of the hydroperoxide group along with an inner sphere electron transfer directly from the iron atom of the Fe(II)$-OH_2$ cofactor. In all, 12 reaction steps are required to get LTA_4 from AA. The initial H_{7proS} abstraction from C_7 of AA turns out to be the rate-determining step of the LTA_4 formation reaction. The addition of the oxygen molecule to C_5 involves a falloff in energy of 38.8 kcal/mol with respect to the H_{7proS} abstraction product, thus providing enough energy for the following reaction steps.

Human-5-LOX contains a broken helix α2 showing a v-like structure, like in Stable-5-LOX. Then, it has a closed conformation, and AA enters (a tail-first entry) and leaves the protein active site exclusively through the channel that involves Trp148. To this aim, Phe422 and Trp148 rotate their side chains to leave free room. The double-ring polar side chain of Trp148 favors the opening of this channel because it can establish a $\pi-\pi$ stacking interaction with Phe152 and a NH$-\pi$ interaction with Arg412. On the other hand, if the helix α2 elongates to give an open conformation, when human-5-LOX is associated with the membrane-embedded FLAP, a change of position of Phe178 and Tyr182 will happen. In this way, the channel shielded by the FY cork in the closed conformation now opens, becoming the most suitable one for AA entering (also a tail-first entry) and leaving the human-5-LOX cavity. It can be assumed that this entrance channel to the human-5-LOX cavity should lie close to the AA site in FLAP.

At this point, we might wonder why the only lipoxygenase whose cellular activity is dependent on a small protein, like FLAP, is 5-LOX. 5-LOX is the only lipoxygenase that produces LTs, key lipid mediators in promoting acute inflammation. Conversely, 12-LOX, 15-LOX, or, again, 5-LOX are needed to

https://doi.org/10.1021/acscatal.3c04954
ACS Catal. 2024, 14, 637−656

generate anti-inflammatory SPMs. We can speculate that the immune system has fundamentally evolved to rapidly protect our body from harmful attacks by triggering acute inflammations and not so much to optimize the subsequent resolution of the inflammations. Thus, the helper protein FLAP exists to provide a very fast delivery of substrates in the case of 5-LOX, so allowing an immediate inflammatory response, whereas the later corresponding resolution driven by other lipoxygenases supposedly need not to be as fast. Admitting the advantages of this defense strategy, the question arises as to whether this preference for the pro-inflammatory function of 5-LOX has weakened its capacity to prevent chronic inflammation more efficiently.

A study of the human-5-LOX mechanism including the membrane-embedded FLAP is now in progress in our laboratory. Meanwhile, we hope that the molecular details described in this work can already help to the development of new therapeutics targeting 5-LOX.

■ ASSOCIATED CONTENT

Supporting Information

The Supporting Information is available free of charge at https://pubs.acs.org/doi/10.1021/acscatal.3c04954.

AA docking calculations; representation of the AA binding mode during the consolidation period of the MD simulation of the human-5-LOX:AA Michaelis complex; time-based representation and histogram of the main H−OH^- distances along the MD simulation of the human-5-LOX:AA Michaelis complex; evolution of the main C−OH^- distances along the MD simulation of the human-5-LOX:AA Michaelis complex; potential energy profiles of the H_{7proS} abstraction from C_7 of AA; definition of the two counterclockwise and clockwise C−C rotations considered in the optimized product of AA oxygenation in C_5; product structure corresponding to the rotation of < (O_1−C_5−C_4−C_3) clockwise; definition of the counterclockwise and clockwise directions of the dihedral rotation < (O_2−O_1−C_5−C_6); evolution of the distances from H_{10proS} and H_{10proR} to the oxygen atom of the OH^- group along the MD simulation of the human-5-LOX:5(*S*)-HpETE Michaelis complex; final potential energy profile for the H_{10proR} abstraction from C_{10} of 5(*S*)-HpETE; 5,6-epoxide ring-closure of the 5(*S*)-HpETE π-heptatrienyl radical following a hydrogen atom transfer from the Fe(II)−OH_2 cofactor; radical 5,6-diol resulting from the tentative mechanism based on the 5,6-epoxide ring-closure of the 5(*S*)-HpETE π-heptatrienyl radical following a hydrogen atom transfer from the Fe(II)−OH_2 cofactor; solvation of AA along its unbinding process from the human-5-LOX pocket through channel A; channel A when it is totally open and ready for the entrance/leaving of AA; potential energy barriers and reaction energies with and without the single-point Grimme Dispersion correction D3(BJ) for the whole human-5-LOX enzymatic process over AA; and parameters developed for 5(*S*)-HpETE (PDF)

Optimized structures for the complete reaction mechanism (TXT)

■ AUTHOR INFORMATION

Corresponding Author

José M. Lluch − *Departament de Química, Universitat Autònoma de Barcelona, Bellaterra 08193 Barcelona, Spain; Institut de Biotecnologia i de Biomedicina (IBB), Universitat Autònoma de Barcelona, Bellaterra 08193 Barcelona, Spain;* orcid.org/0000-0002-7536-1869; Email: JoseMaria.Lluch@uab.cat

Authors

Alejandro Cruz − *Departament de Química, Universitat Autònoma de Barcelona, Bellaterra 08193 Barcelona, Spain;* orcid.org/0000-0003-0928-0718

Àngels González-Lafont − *Departament de Química, Universitat Autònoma de Barcelona, Bellaterra 08193 Barcelona, Spain; Institut de Biotecnologia i de Biomedicina (IBB), Universitat Autònoma de Barcelona, Bellaterra 08193 Barcelona, Spain;* orcid.org/0000-0003-0729-2483

Complete contact information is available at: https://pubs.acs.org/10.1021/acscatal.3c04954

Author Contributions

The manuscript was written through the contributions of all authors. All authors have given approval for the final version of the manuscript.

Notes

The authors declare no competing financial interest.

■ ACKNOWLEDGMENTS

This work was supported by the "Ministerio de Ciencia e Innovación" of Spain through project PID2020-113764GB-I00. We acknowledge CSUC ("Consorci de Serveis Universitaris de Catalunya") for the allocation of computer resources.

■ REFERENCES

(1) Furman, D.; Campisi, J.; Verdin, E.; Carrera-Bastos, P.; Targ, S.; Franceschi, C.; Ferrucci, L.; Gilroy, D. W.; Fasano, A.; Miller, G. W.; Miller, A. H.; Mantovani, A.; Weyand, C. M.; Barzilai, N.; Goronzy, J. J.; Rando, T. A.; Effros, R. B.; Lucia, A.; Kleinstreuer, N.; Slavich, G. M. Chronic Inflammation in the Etiology of Disease across the Life Span. *Nat. Med.* **2019**, *25* (12), 1822−1832.

(2) Chiang, N.; Serhan, C. N. Structural Elucidation and Physiologic Functions of Specialized Pro-Resolving Mediators and Their Receptors. *Mol. Aspects Med.* **2017**, *58*, 114−129.

(3) Chen, L.; Deng, H.; Cui, H.; Fang, J.; Zuo, Z.; Deng, J.; Li, Y.; Wang, X.; Zhao, L.; Chen, L.; Deng, H.; Cui, H.; Fang, J.; Zuo, Z.; Deng, J.; Li, Y.; Wang, X.; Zhao, L. Inflammatory Responses and Inflammation-Associated Diseases in Organs. *Oncotarget* **2017**, *9* (6), 7204−7218.

(4) Serhan, C. N.; Petasis, N. A. Resolvins and Protectins in Inflammation Resolution. *Chem. Rev.* **2011**, *111* (10), 5922−5943.

(5) Buckley, C. D.; Gilroy, D. W.; Serhan, C. N. Proresolving Lipid Mediators and Mechanisms in the Resolution of Acute Inflammation. *Immunity* **2014**, *40* (3), 315−327.

(6) Serhan, C. N. Treating Inflammation and Infection in the 21st Century: New Hints from Decoding Resolution Mediators and Mechanisms. *FASEB J.* **2017**, *31*, 1273−1288.

(7) Fattori, V.; Zaninelli, T. H.; Rasquel-Oliveira, F. S.; Casagrande, R.; Verri, W. A. Specialized Pro-Resolving Lipid Mediators: A New Class of Non-Immunosuppressive and Non-Opioid Analgesic Drugs. *Pharmacol. Res.* **2020**, *151*, 104549.

(8) Serhan, C. N.; Gupta, S. K.; Perretti, M.; Godson, C.; Brennan, E.; Li, Y.; Soehnlein, O.; Shimizu, T.; Werz, O.; Chiurchiù, V.; Azzi, A.; Dubourdeau, M.; Gupta, S. S.; Schopohl, P.; Hoch, M.; Gjorgevikj,

D.; Khan, F. M.; Brauer, D.; Tripathi, A.; Cesnulevicius, K.; Lescheid, D.; Schultz, M.; Särndahl, E.; Repsilber, D.; Kruse, R.; Sala, A.; Haeggström, J. Z.; Levy, B. D.; Filep, J. G.; Wolkenhauer, O. The Atlas of Inflammation Resolution (AIR). *Mol. Aspects Med.* **2020**, *74*, 100894.
(9) *Fundamentals of Inflammation*; Serhan, C. N., Ward, P. A., Gilroy, D. W., Eds.; Cambridge University Press: Cambridge, UK, 2010.
(10) Serhan, C. N.; Hamberg, M.; Samuelsson, B. Trihydroxytetraenes: A Novel Series of Compounds Formed from Arachidonic Acid in Human Leukocytes. *Biochem. Biophys. Res. Commun.* **1984**, *118* (3), 943−949.
(11) Catalano, A.; Procopio, A. New Aspects on the Role of Lipoxygenases in Cancer Progression. *Histol. Histopathol.* **2005**, *20* (3), 969−975.
(12) Dobrian, A. D.; Lieb, D. C.; Cole, B. K.; Taylor-Fishwick, D. A.; Chakrabarti, S. K.; Nadler, J. L. Functional and Pathological Roles of the 12- and 15-Lipoxygenases. *Prog. Lipid Res.* **2011**, *50* (1), 115−131.
(13) Haeggström, J. Z.; Funk, C. D. Lipoxygenase and Leukotriene Pathways: Biochemistry, Biology, and Roles in Disease. *Chem. Rev.* **2011**, *111* (10), 5866−5896.
(14) Joo, Y. C.; Oh, D. K. Lipoxygenases: Potential Starting Biocatalysts for the Synthesis of Signaling Compounds. *Biotechnol. Adv.* **2012**, *30* (6), 1524−1532.
(15) Steinhilber, D. *Lipoxygenases in Inflammation*; Springer International Publishing: Switzerland, 2016.
(16) Smyrniotis, C. J.; Barbour, S. R.; Xia, Z.; Hixon, M. S.; Holman, T. R. ATP Allosterically Activates the Human 5-Lipoxygenase Molecular Mechanism of Arachidonic Acid and 5(S)-Hydroperoxy-6(E), 8(Z), 11(Z), 14(Z)-Eicosatetraenoic Acid. *Biochemistry* **2014**, *53* (27), 4407−4419.
(17) Wan, M.; Tang, X.; Stsiapanava, A.; Haeggström, J. Z. Biosynthesis of Leukotriene B4. *Semin. Immunol.* **2017**, *33*, 3−15.
(18) Canyelles-Niño, M.; González-Lafont, À.; Lluch, J. M. Theoretical Characterization of the Step-by-Step Mechanism of Conversion of Leukotriene A4 to Leukotriene B4 Catalysed by the Enzyme Leukotriene A4 Hydrolase. *Int. J. Mol. Sci.* **2022**, *23* (6), 3140.
(19) Gilbert, N. C.; Bartlett, S. G.; Waight, M. T.; Neau, D. B.; Boeglin, W. E.; Brash, A. R.; Newcomer, M. E. The Structure of Human 5-Lipoxygenase. *Science* **2011**, *331* (6014), 217−219.
(20) Gallegos, E. M.; Reed, T. D.; Mathes, F. A.; Guevara, N. V.; Neau, D. B.; Huang, W.; Newcomer, M. E.; Gilbert, N. C. Helical Remodeling Augments 5-Lipoxygenase Activity in the Synthesis of Proinflammatory Mediators. *J. Biol. Chem.* **2022**, *298* (9), 102282.
(21) Mitra, S.; Bartlett, S. G.; Newcomer, M. E. Identification of the Substrate Access Portal of 5-Lipoxygenase. *Biochemistry* **2015**, *54* (41), 6333−6342.
(22) Haeggström, J. Z.; Newcomer, M. E. Structures of Leukotriene Biosynthetic Enzymes and Development of New Therapeutics. *Annu. Rev. Pharmacol. Toxicol.* **2023**, *63*, 407−428.
(23) Gilbert, N. C.; Newcomer, M. E.; Werz, O. Untangling the Web of 5-Lipoxygenase-Derived Products from a Molecular and Structural Perspective: The Battle between pro- and Anti-Inflammatory Lipid Mediators. *Biochem. Pharmacol.* **2021**, *193*, 114759.
(24) Saura, P.; Maréchal, J. D.; Masgrau, L.; Lluch, J. M.; González-Lafont, À. Computational Insight into the Catalytic Implication of Head/Tail-First Orientation of Arachidonic Acid in Human 5-Lipoxygenase: Consequences for the Positional Specificity of Oxygenation. *Phys. Chem. Chem. Phys.* **2016**, *18* (33), 23017−23035.
(25) Jumper, J.; Evans, R.; Pritzel, A.; Green, T.; Figurnov, M.; Ronneberger, O.; Tunyasuvunakool, K.; Bates, R.; Žídek, A.; Potapenko, A.; Bridgland, A.; Meyer, C.; Kohl, S. A. A.; Ballard, A. J.; Cowie, A.; Romera-Paredes, B.; Nikolov, S.; Jain, R.; Adler, J.; Back, T.; Petersen, S.; Reiman, D.; Clancy, E.; Zielinski, M.; Steinegger, M.; Pacholska, M.; Berghammer, T.; Bodenstein, S.; Silver, D.; Vinyals, O.; Senior, A. W.; Kavukcuoglu, K.; Kohli, P.; Hassabis, D. Highly Accurate Protein Structure Prediction with AlphaFold. *Nature* **2021**, *596* (7873), 583−589.
(26) Varadi, M.; Anyango, S.; Deshpande, M.; Nair, S.; Natassia, C.; Yordanova, G.; Yuan, D.; Stroe, O.; Wood, G.; Laydon, A.; Žídek, A.; Green, T.; Tunyasuvunakool, K.; Petersen, S.; Jumper, J.; Clancy, E.; Green, R.; Vora, A.; Lutfi, M.; Figurnov, M.; Cowie, A.; Hobbs, N.; Kohli, P.; Kleywegt, G.; Birney, E.; Hassabis, D.; Velankar, S. AlphaFold Protein Structure Database: Massively Expanding the Structural Coverage of Protein-Sequence Space with High-Accuracy Models. *Nucleic Acids Res.* **2022**, *50* (D1), D439−D444.
(27) Gordon, J. C.; Myers, J. B.; Folta, T.; Shoja, V.; Heath, L. S.; Onufriev, A. H++: A Server for Estimating PKas and Adding Missing Hydrogens to Macromolecules. *Nucleic Acids Res.* **2005**, *33* (suppl_2), W368−W371.
(28) Anandakrishnan, R.; Aguilar, B.; Onufriev, A. V. H++ 3.0: Automating PK Prediction and the Preparation of Biomolecular Structures for Atomistic Molecular Modeling and Simulations. *Nucleic Acids Res.* **2012**, *40* (W1), W537−W541.
(29) Jones, G.; Willett, P.; Glen, R. C.; Leach, A. R.; Taylor, R. Development and validation of a genetic algorithm for flexible docking. *J. Mol. Biol.* **1997**, *267* (3), 727−748.
(30) Case, D. A.; Belfon, K.; Ben-Shalom, I. Y.; Brozell, S. R.; Cerutti, D. S.; Cheatham, T. E., III; Cruzeiro, V. W. D.; Darden, T. A.; Duke, R. E.; Giambasu, G.; Gilson, M. K.; Gohlke, H.; Goetz, A. W.; Harris, R.; Izadi, S.; Izmailov, S. A.; Kasavajhala, K.; Kovalenko, A.; Krasny, R.; Kurtzman, T.; Lee, T. S.; LeGrand, S.; Li, P.; Lin, C.; Liu, J.; Luchko, T.; Luo, R.; Man, V.; Merz, K. M.; Miao, Y.; Mikhailovskii, O.; Monard, G.; Nguyen, H.; Onufriev, A.; Pan, F.; Pantano, S.; Qi, R.; Roe, D. R.; Roitberg, A.; Sagui, C.; Schott-Verdugo, S.; Shen, J.; Simmerling, C. L.; Skrynnikov, N. R.; Smith, J.; Swails, J.; Walker, R. C.; Wang, J.; Wilson, L.; Wolf, R. M.; Wu, X.; Xiong, Y.; Xue, Y.; York, D. M.; Kollman, P. A. *AMBER 2020*; University of California: San Francisco, 2020.
(31) Maier, J. A.; Martinez, C.; Kasavajhala, K.; Wickstrom, L.; Hauser, K. E.; Simmerling, C. Ff14SB: Improving the Accuracy of Protein Side Chain and Backbone Parameters from Ff99SB. *J. Chem. Theory Comput.* **2015**, *11* (8), 3696−3713.
(32) Tosco, P. A Mechanistic Hypothesis for the Aspirin-Induced Switch in Lipid Mediator Production by Cyclooxygenase-2. *J. Am. Chem. Soc.* **2013**, *135* (28), 10404−10410.
(33) Ivanov, I.; Golovanov, A. B.; Ferretti, C.; Canyelles-Niño, M.; Heydeck, D.; Stehling, S.; Lluch, J. M.; González-Lafont, À.; Kühn, H. Mutations of Triad Determinants Changes the Substrate Alignment at the Catalytic Center of Human ALOX5. *ACS Chem. Biol.* **2019**, *14* (12), 2768−2782.
(34) Wang, J.; Wolf, R. M.; Caldwell, J. W.; Kollman, P. A.; Case, D. A. Development and Testing of a General Amber Force Field. *J. Comput. Chem.* **2004**, *25* (9), 1157−1174.
(35) Bayly, C. I.; Cieplak, P.; Cornell, W.; Kollman, P. A. A Well-Behaved Electrostatic Potential Based Method Using Charge Restraints for Deriving Atomic Charges: The RESP Model. *J. Phys. Chem.* **1993**, *97* (40), 10269−10280.
(36) Jorgensen, W. L.; Chandrasekhar, J.; Madura, J. D.; Impey, R. W.; Klein, M. L. Comparison of Simple Potential Functions for Simulating Liquid Water. *J. Chem. Phys.* **1983**, *79* (2), 926−935.
(37) Salomon-Ferrer, R.; Götz, A. W.; Poole, D.; Le Grand, S.; Walker, R. C. Routine Microsecond Molecular Dynamics Simulations with AMBER on GPUs. 2. Explicit Solvent Particle Mesh Ewald. *J. Chem. Theory Comput.* **2013**, *9* (9), 3878−3888.
(38) Le Grand, S.; Götz, A. W.; Walker, R. C. SPFP: Speed without Compromise—A Mixed Precision Model for GPU Accelerated Molecular Dynamics Simulations. *Comput. Phys. Commun.* **2013**, *184* (2), 374−380.
(39) Leach, A. R. *Molecular Modelling: Principles and Applications*, 2nd ed.; Prentice Hall: UK, 2001.
(40) Berendsen, H. J. C.; Postma, J. P. M.; van Gunsteren, W. F.; DiNola, A.; Haak, J. R. Molecular Dynamics with Coupling to an External Bath. *J. Chem. Phys.* **1984**, *81* (8), 3684−3690.
(41) Ryckaert, J.-P.; Ciccotti, G.; Berendsen, H. J. C. Numerical Integration of the Cartesian Equations of Motion of a System with

https://doi.org/10.1021/acscatal.3c04954
ACS Catal. 2024, 14, 637−656

Constraints: Molecular Dynamics of n-Alkanes. *J. Comput. Phys.* **1977**, *23* (3), 327−341.
(42) Darden, T.; York, D.; Pedersen, L. Particle mesh Ewald: An *N*·log(*N*) method for Ewald sums in large systems. *J. Chem. Phys.* **1993**, *98* (12), 10089−10092.
(43) Essmann, U.; Perera, L.; Berkowitz, M. L.; Darden, T.; Lee, H.; Pedersen, L. G. A Smooth Particle Mesh Ewald Method. *J. Chem. Phys.* **1995**, *103* (19), 8577−8593.
(44) Sherwood, P.; De Vries, A. H.; Guest, M. F.; Schreckenbach, G.; Catlow, C. A.; French, S. A.; Sokol, A. A.; Bromley, S. T.; Thiel, W.; Turner, A. J.; Billeter, S.; Terstegen, F.; Thiel, S.; Kendrick, J.; Rogers, S. C.; Casci, J.; Watson, M.; King, F.; Karlsen, E.; Sjøvoll, M.; Fahmi, A.; Schäfer, A.; Lennartz, C. QUASI: A General Purpose Implementation of the QM/MM Approach and Its Application to Problems in Catalysis. *J. Mol. Struct.: THEOCHEM* **2003**, *632* (1−3), 1−28.
(45) Metz, S.; Kästner, J.; Sokol, A. A.; Keal, T. W.; Sherwood, P. ChemShell-a Modular Software Package for QM/MM Simulations. *WIREs Comput. Mol. Sci.* **2014**, *4* (2), 101−110.
(46) Ahlrichs, R.; Bär, M.; Häser, M.; Horn, H.; Kölmel, C. Electronic Structure Calculations on Workstation Computers: The Program System Turbomole. *Chem. Phys. Lett.* **1989**, *162* (3), 165−169.
(47) Smith, W.; Forester, T. R. DL_POLY_2.0: A general-purpose parallel molecular dynamics simulation package. *J. Mol. Graph.* **1996**, *14* (3), 136−141.
(48) Bakowies, D.; Thiel, W. Hybrid Models for Combined Quantum Mechanical and Molecular Mechanical Approaches. *J. Phys. Chem.* **1996**, *100* (25), 10580−10594.
(49) Senn, H. M.; Thiel, W. QM/MM Methods for Biomolecular Systems. *Angew. Chem., Int. Ed.* **2009**, *48* (7), 1198−1229.
(50) De Vries, A. H.; Sherwood, P.; Collins, S. J.; Rigby, A. M.; Rigutto, M.; Kramer, G. J. Zeolite Structure and Reactivity by Combined Quantum-Chemical-Classical Calculations. *J. Phys. Chem. B* **1999**, *103* (29), 6133−6141.
(51) Liu, D. C.; Nocedal, J. On the Limited Memory BFGS Method for Large Scale Optimization. *Math. Program.* **1989**, *45* (1−3), 503−528.
(52) Nocedal, J. Updating Quasi-Newton Matrices with Limited Storage. *Math. Comput.* **1980**, *35* (151), 773−782.
(53) Kästner, J.; Carr, J. M.; Keal, T. W.; Thiel, W.; Wander, A.; Sherwood, P. DL-FIND: An Open-Source Geometry Optimizer for Atomistic Simulations*. *J. Phys. Chem. A* **2009**, *113* (43), 11856−11865.
(54) Becke, A. D. Density-Functional Thermochemistry. III. The Role of Exact Exchange. *J. Chem. Phys.* **1993**, *98* (7), 5648−5652.
(55) Hariharan, P. C.; Pople, J. A. The Influence of Polarization Functions on Molecular Orbital Hydrogenation Energies. *Theor. Chim. Acta* **1973**, *28* (3), 213−222.
(56) Hay, P. J.; Wadt, W. R. Ab Initio Effective Core Potentials for Molecular Calculations. Potentials for the Transition Metal Atoms Sc to Hg. *J. Chem. Phys.* **1985**, *82* (1), 270−283.
(57) Saura, P.; Suardíaz, R.; Masgrau, L.; Lluch, J. M.; González-Lafont, À. Unraveling How Enzymes Can Use Bulky Residues to Drive Site-Selective c-h Activation: The Case of Mammalian Lipoxygenases Catalyzing Arachidonic Acid Oxidation. *ACS Catal.* **2014**, *4* (12), 4351−4363.
(58) Soler, J.; Saura, P.; García-López, D.; Masgrau, L.; Lluch, J. M.; González-Lafont, À. How Can Linoleic Acid Be the Preferential Substrate of the Enzyme 15-Lipoxygenase-1? A QM/MM Approach. *J. Phys. Chem. B* **2016**, *120* (8), 1950−1960.
(59) Saura, P.; Kaganer, I.; Heydeck, D.; Lluch, J. M.; Kühn, H.; González-Lafont, À. Mutagenesis of Sequence Determinants of Truncated Porcine ALOX15 Induces Changes in the Reaction Specificity by Altering the Catalytic Mechanism of Initial Hydrogen Abstraction. *Chem.—Eur. J.* **2018**, *24* (4), 962−973.
(60) Adel, S.; Karst, F.; González-Lafont, À.; Pekárová, M.; Saura, P.; Masgrau, L.; Lluch, J. M.; Stehling, S.; Horn, T.; Kuhn, H.; Heydeck, D. Evolutionary Alteration of ALOX15 Specificity Optimizes the Biosynthesis of Antiinflammatory and Proresolving Lipoxins. *Proc. Natl. Acad. Sci. U.S.A.* **2016**, *113* (30), E4266−E4275.
(61) Grimme, S.; Antony, J.; Ehrlich, S.; Krieg, H. A Consistent and Accurate Ab Initio Parametrization of Density Functional Dispersion Correction (DFT-D) for the 94 Elements H-Pu. *J. Chem. Phys.* **2010**, *132* (15), 154104.
(62) Suardíaz, R.; Jambrina, P. G.; Masgrau, L.; González-Lafont, À.; Rosta, E.; Lluch, J. M. Understanding the Mechanism of the Hydrogen Abstraction from Arachidonic Acid Catalyzed by the Human Enzyme 15-Lipoxygenase-2. A Quantum Mechanics/Molecular Mechanics Free Energy Simulation. *J. Chem. Theory Comput.* **2016**, *12* (4), 2079−2090.
(63) Chovancova, E.; Pavelka, A.; Benes, P.; Strnad, O.; Brezovsky, J.; Kozlikova, B.; Gora, A.; Sustr, V.; Klvana, M.; Medek, P.; Biedermannova, L.; Sochor, J.; Damborsky, J. CAVER 3.0: A Tool for the Analysis of Transport Pathways in Dynamic Protein Structures. *PLoS Comput. Biol.* **2012**, *8* (10), No. e1002708.
(64) *The PyMOL Molecular Graphics System*, version 2.0; Schrödinger, LLC.
(65) Humphrey, W.; Dalke, A.; Schulten, K. VMD: Visual Molecular Dynamics. *J. Mol. Graph.* **1996**, *14* (1), 33−38.
(66) Pettersen, E. F.; Goddard, T. D.; Huang, C. C.; Couch, G. S.; Greenblatt, D. M.; Meng, E. C.; Ferrin, T. E. UCSF Chimera - A Visualization System for Exploratory Research and Analysis. *J. Comput. Chem.* **2004**, *25* (13), 1605−1612.
(67) Park, S.; Khalili-Araghi, F.; Tajkhorshid, E.; Schulten, K. Free Energy Calculation from Steered Molecular Dynamics Simulations Using Jarzynski's Equality. *J. Chem. Phys.* **2003**, *119* (6), 3559−3566.
(68) Jarzynski, C. Nonequilibrium Equality for Free Energy Differences. *Phys. Rev. Lett.* **1997**, *78* (14), 2690−2693.
(69) Jensen, M.; Park, S.; Tajkhorshid, E.; Schulten, K. Energetics of Glycerol Conduction through Aquaglyceroporin GlpF. *Proc. Natl. Acad. Sci. U.S.A.* **2002**, *99* (10), 6731−6736.
(70) Hummer, G. Fast-Growth Thermodynamic Integration: Error and Efficiency Analysis. *J. Chem. Phys.* **2001**, *114* (17), 7330−7337.
(71) Schwarz, K.; Walther, M.; Anton, M.; Gerth, C.; Feussner, I.; Kuhn, H. Structural Basis for Lipoxygenase Specificity. *J. Biol. Chem.* **2001**, *276* (1), 773−779.
(72) Perry, S. C.; Horn, T.; Tourdot, B. E.; Yamaguchi, A.; Kalyanaraman, C.; Conrad, W. S.; Akinkugbe, O.; Holinstat, M.; Jacobson, M. P.; Holman, T. R. Role of Human 15-Lipoxygenase-2 in the Biosynthesis of the Lipoxin Intermediate, 5S, 15S-Dihpete, Implicated with the Altered Positional Specificity of Human 15-Lipoxygenase-1. *Biochemistry* **2020**, *59* (42), 4118−4130.
(73) Waheed, S. O.; Ramanan, R.; Chaturvedi, S. S.; Lehnert, N.; Schofield, C. J.; Christov, C. Z.; Karabencheva-Christova, T. G. Role of Structural Dynamics in Selectivity and Mechanism of Non-Heme Fe(II) and 2-Oxoglutarate-Dependent Oxygenases Involved in DNA Repair. *ACS Cent. Sci.* **2020**, *6* (5), 795−814.
(74) Torabifard, H.; Cisneros, G. A. Computational Investigation of O2 Diffusion through an Intra-Molecular Tunnel in AlkB; Influence of Polarization on O2 Transport. *Chem. Sci.* **2017**, *8* (9), 6230−6238.
(75) Gadnayak, A.; Dehury, B.; Nayak, A.; Jena, S.; Sahoo, A.; Panda, P. C.; Ray, A.; Nayak, S. 'Mechanistic Insights into 5-Lipoxygenase Inhibition by Active Principles Derived from Essential Oils of Curcuma Species: Molecular Docking, ADMET Analysis and Molecular Dynamic Simulation Study. *PLoS One* **2022**, *17* (7), No. e0271956.

https://doi.org/10.1021/acscatal.3c04954
ACS Catal. 2024, 14, 637−656